

# 3-D Millimeter-Wave Statistical Channel Model for 5G Wireless System Design

Mathew K. Samimi, *Student Member, IEEE*, and Theodore S. Rappaport, *Fellow, IEEE*

**Abstract**—This paper presents a 3-D statistical channel impulse response (IR) model for urban line of sight (LOS) and non-LOS channels developed from 28- and 73-GHz ultrawideband propagation measurements in New York City, useful in the design of 5G wireless systems that will operate in both the ultra-high frequency/microwave and millimeter-wave (mmWave) spectrum to increase channel capacities. A 3GPP-like stochastic IR channel model is developed from measured power delay profiles, angle of departure, and angle of arrival power spectra. The extracted statistics are used to implement a channel model and simulator capable of generating 3-D mmWave temporal and spatial channel parameters for arbitrary mmWave carrier frequency, signal bandwidth, and antenna beamwidth. The model presented here faithfully reproduces realistic IRs of measured urban channels, supporting air interface design of mmWave transceivers, filters, and multi-element antenna arrays.

**Index Terms**—Channel model, 5G, impulse response (IR), millimeter-wave (mmWave) propagation, multipath, 73 GHz, spatial channel model (SCM), spatial lobe (SL), statistical simulator, 3-D ray-tracing, time cluster (TC), time cluster spatial lobe (TCSL), 28 GHz.

## I. INTRODUCTION

THE next generation of wireless communications will use systems operating from 500 MHz to 100 GHz [1], [2]. Today's cellular systems use ultrahigh frequency (UHF) and Microwave bands exploiting multi-user multiple-input multiple-output (MU-MIMO) [3], [4], coordinated multipoint systems [5]–[7], heterogeneous networks [3], [7], and carrier aggregation [8]. However, the incredible demand for broadband wireless mobility will be supplied by moving up to the millimeter-wave (mmWave) spectrum, where a massive amount of raw bandwidth exists [9], [10], and therefore, the design of 5G cellular networks requires channel models that characterize the sub-6 GHz and mmWave spectrum to perform multi-band system-level simulations.

A number of mmWave bands are currently being considered for global 5G networks. The 28- and 73-GHz frequency bands for outdoor communications are attractive, as the attenuation loss induced from atmospheric absorption

Manuscript received December 29, 2015; revised April 3, 2016; accepted May 14, 2016. Date of publication June 25, 2016; date of current version July 7, 2016. This work was supported by the National Science Foundation under Grant 1302336, Grant 1320472, and Grant 1555332. Portions of this work were published in [16], [35], and [38].

The authors are with NYU WIRELESS, New York University Tandon School of Engineering, Brooklyn, NY 11201 USA (e-mail: mks@nyu.edu; tsr@nyu.edu).

Color versions of one or more of the figures in this paper are available online at <http://ieeexplore.ieee.org>.

Digital Object Identifier 10.1109/TMTT.2016.2574851

is minor (much less than 0.1 dB) over a realistic mmWave cell radius of 200 m [11], while it is significantly higher at 60 GHz ( $\sim 4$  dB/200 m). Also, the Federal Communications Commission has recently issued new rulemakings to bring these bands into service [12]. The 38- and 60-GHz outdoor ultrawideband channels have been extensively studied at the UT Austin campus [13], and more recently at 28 and 73 GHz at New York University using directional antennas for outdoor mobile communications [14].

This work presents a statistical spatial channel model (SSCM) developed using the time cluster–spatial lobe (TCSL) approach, which augments the existing UHF 3GPP model through the additional model parameters of directional RMS lobe angular spreads for spatial lobes (SLs) [15]–[17]. The TCSL modeling framework is shown here to faithfully reproduce the first- and second-order time and angular statistics of measured channels that use directional antennas in mmWave bands [16], and is suitable for 5G system design of filters, electrically-steered antenna arrays, and mmWave transceivers. The SSCM presented here is based on extensive propagation measurements carried out from 2011 through 2015, and generates multipath parameters for omnidirectional and directional channel impulse responses (CIRs) for links between a transmitter (TX) and receiver (RX) as well as over a local area.

We demonstrate that the IR model can be generalized to arbitrary environments and antenna beamwidths to create directional channel IRs in other mmWave frequency bands. The IR channel model is first developed for four distinct frequency scenarios: 1) the 28-GHz non-line of sight (NLOS) urban channel; 2) the 73-GHz NLOS urban channel; 3) the combined 28–73-GHz urban line of sight (LOS) channel; and 4) the combined 28–73-GHz urban NLOS channel. The 28- and 73-GHz LOS statistics were lumped into one combined data set to extract combined 28- and 73-GHz statistics, motivated by the fact that measurements clearly show that these two frequencies have virtually identical path loss exponents (PLEs) close to free space ( $n = 2$ ), and have virtually the same values of average number of resolvable multipath components [12]. The similarity in channel characteristics for LOS channels over mmWave frequencies provides motivation to combine the data to provide a greater statistical sample size when deriving the model statistics.

The SSCM presented in this paper has been implemented using a MATLAB program and is publicly available as a freely downloadable software package suitable for link and system-level simulations [18].

The contributions in this paper include the following.

- 1) A 3-D mmWave SSCM for generating CIRs at particular distances and over local areas based on the TCSL modeling framework, which extends the 3GPP model through directional RMS lobe angular spreads while keeping consistent with the 3GPP modeling framework. The SSCM has been validated using published measurements between 28 and 73 GHz and can be used for arbitrary carrier frequency between 6 and 100 GHz, RF signal bandwidths up to 800 MHz, and arbitrary antenna beamwidths greater than 7°.
- 2) A modeling extension to enable the spatial consistency in multi-user system-level simulations that account for the birth and death of time clusters (TCs) and spatial lobes (SLs) at mmWave frequencies in a track- or grid-based scenario, using the statistical spatial autocorrelation for the number of TCs and SLs.

#### A. Millimeter-Wave Channel Characterization

In the 1990s, mmWave channels were studied and modeled especially for LOS communications in urban macrocellular [19]–[21] and short-range indoor environments [22], [23], including important wideband channel models [24]–[26]. In the past few years, the 28-, 38-, and 70–80-GHz frequency bands have become important candidates for mmWave mobile communications [10], [12], [27].

Recently, mmWave propagation measurement campaigns have been conducted in indoor and dense urban outdoor environments [11], [12], [28]–[31]. Previous results yielded directional and omnidirectional path loss models in dense urban LOS and NLOS environments [12], [27], [32], [33], temporal and spatial channel parameters, such as cluster and angular spread statistics, and statistical distributions at 28 and 73 GHz based on measurements and ray-tracing [1], [2], [14], [29], [32], [34]–[37]. Sun *et al.* [33] demonstrate that urban microcell (UMi) NLOS omnidirectional PLEs range between 2.9 and 3.4, with corresponding shadow factors ranging from 2.9 to 8.6 dB, when using the 1-m close-in (CI) free space reference distance path loss model for carrier frequencies of 2.9, 28, 29, and 73 GHz. The first- and second-order simulated directional RMS delay spreads were shown to agree well with measured directional RMS delay spreads obtained over different antenna half-power beamwidths (HPBWs) and mmWave bands ranging from 28 to 73 GHz, as shown in Fig. 19 and [16].

A 3-D SSCM for LOS and NLOS mobile communications [16], [38] reproduced measurements of wideband power delay profiles (PDPs) and 3-D angle of departure (AOD) and angle of arrival (AOA) power angular spectra for multi-frequency and arbitrary antenna beamwidth [16]. Initial MIMO network simulations were carried out in [39] using a 2-D wideband mmWave statistical simulator developed from 28-GHz wideband propagation measurements [40], and showed orders of magnitude increase in data rates compared with current 3G and 4G LTE mobile systems when using spatial multiplexing and beamforming at the base station (BS) for LOS and NLOS urban environments.

#### B. Popular Statistical and Analytical Channel Models

1) *3GPP and WINNER II Models:* The geometry-based stochastic 3GPP and WINNER II spatial channel models (SCMs) [41], [42] follow a system-level approach, suitable for link-level or system-level simulations to estimate realistic channels between a BS, and one or more user equipments (UEs), that account for empirical correlations between large-scale parameters. The large-scale parameters denote the omnidirectional RMS delay spread (DS), the azimuth spread (AS), the shadow fading (SF), and the Rician K-factor (for LOS channels), and were shown to exhibit significant correlation [43] for a given base-to-mobile link. The spatial cross-correlation coefficients between two mobile stations (MSs) for the DS and AS, DS and SF, and AS and SF are set to +0.5, -0.6, and -0.6, respectively [41], [44], in the 3GPP models, based on work in [43]. The 3GPP model also specifies a spatial autocorrelation coefficient of +0.5 for the shadow fading experienced by two MSs, but does not specify the distance range over which the shadow fading correlation is applicable [41]. In the WINNER SCM, the spatial cross-correlation coefficients between two MSs separated by a distance  $d_{\text{MS}}$  are modeled using a decaying exponential function, which is parameterized using the correlation distance parameter. The correlation distance between two large-scale parameters is the distance at which the cross-correlation coefficient is equal to 0.37 (1/e), and the values are provided in [42, Table 4-5], with typical correlation distances ranging from 9 to 14 m for the UMi scenario. In both SCMs, the large-scale parameters are generated using correlated Gaussian random variables [41] to recreate the measured joint statistics.

The models make the simplifying assumption that each multipath component can be represented by a planar wavefront, characterized by small-scale parameters such as path delays, powers, AOAs, and AODs, extracted from measurement-based statistical distributions. Typical IRs in an NLOS UMi environment are modeled using a clustered delay line model using a fixed number of paths, with  $N = 6$  paths [41], or  $N = 16$  paths [42], where each path is further subdivided into  $M = 20$  equal power rays. Note that the 3GPP and WINNER models adopt different terminologies to refer to a group of traveling multipaths. The 3GPP model defines a *path* as a time-delayed multipath copy of the transmitted signal that is subdivided into 20 rays [41], where all rays have the same path delay but slight AOD and AOA offsets. In contrast, the WINNER II model defines a *cluster* as a propagation path diffused in space, either or both in delay and angle domains, and a number of rays (typically 20) constitute a cluster, where the two strongest clusters are subdivided into three subclusters with intra-cluster delays of 0, 5, and 10 ns [42].

Current 3GPP and WINNER [41], [42] models make the presumption that clusters are characterized by a joint delay-angle probability density function, such that a group of traveling multipaths must depart and arrive from a unique AOD-AOA angle combination centered around a mean propagation delay [32]. This was not born out by extensive mmWave field measurements [17]. Cluster properties are usually obtained from high-resolution parameter extraction algorithms, like the SAGE [45] or KPowerMeans [46]

algorithms, which require measurements acquired with multi-element antenna arrays. The small-scale fading statistics of a path (or cluster) are recreated from the superposition of the path rays, by taking the coherent sum of complex ray amplitudes, each subject to Doppler shifts. The path gain amplitudes are assumed to be Rician and Rayleigh [41], [44] in LOS and NLOS UMi environments, respectively, and the phases of each ray are generated using a uniform distribution between 0 and  $2\pi$  [41]. These widespread SCMs were used to design today's 3G and 4G systems, based on 1–6 GHz propagation measurements, for RF signal bandwidths spanning 5–100 MHz (20-ns smallest time resolution) [41], [42].

2) *COST 2100 Models*: The COST 2100 models follow a cluster-level approach, where clusters (e.g., scattering objects) are dropped in a simulated environment and can interact with one or more mobile terminals using the concept of *visibility region*. The visibility region as defined in the COST 2100 model [47], [48] is a key concept of geometric and stochastic propagation models, and represents the space- or time-span over which a group of traveling multipath components are present at a generic radio terminal antenna [48]. Spatial consistency is enabled through the use of visibility regions associated with each cluster of multipath components. One or more clusters of rays are assigned to a visibility region, whose size varies as a mobile terminal moves, thereby allowing for spatial consistency in a simulated environment. Spatial consistency refers to smooth channel transitions between closely separated mobile terminals that experience a similar, but slightly different, scattering environment. Ignoring spatial consistency can overestimate the performance of spatial multi-antenna techniques [37]. The COST 2100 models assume Rayleigh fading for path gain amplitudes in NLOS environments to recreate the statistics of small-scale fading. In the COST 2100 model, the time delay of a multipath component is the sum of three delays: 1) the BS-to-scatterer delay; 2) the MS-to-scatterer delay; and 3) the cluster-link delay [47].

3) *MiWEBA Models*: The mmWave Evolution for Backhaul and Access (MiWEBA) models [14] employ a quasi-deterministic channel model to characterize the 60-GHz outdoor multipath channels, by considering the superposition of a few strong deterministic paths and several relatively weak random rays. The deterministic rays are modeled using Friis' free space path loss equation and path-length geometry determined from the TX and RX heights and the T-R separation distance, while the properties of weaker random rays are generated from measurement-based statistical distributions. These models are based on wideband propagation measurements at 60 GHz and directional antennas. The models are useful for system-level simulations and network access capacity analyses. The model assumes that random clusters arrive with a Poisson process, with exponentially distributed inter-arrival times, while random cluster amplitudes are Rayleigh distributed, with phases generated from independent and identically distributed uniform distributions between 0 and  $2\pi$  [14]. These models also account for blockage by vehicles and humans by specifying the probability of blockage for deterministic rays and random rays.

4) *METIS Models*: The METIS models employ a combination of map-based and stochastic channel models to estimate path amplitudes, and are suitable for evaluating massive MIMO and advanced beamforming algorithms through Monte-Carlo simulations [37]. The model uses ray-tracing techniques to obtain large-scale fading characteristics for a site-specific environment, and measurement-based results to model the small-scale fading statistics. The small-scale statistics are generated following the 3GPP and WINNER modeling approaches.

5) *SIRCIM/SMRCIM Model*: A measurement-based statistical indoor radio-channel impulse response (IR) model (SIRCIM) and outdoor mobile simulator (SMRCIM) were successfully implemented from many thousands of collected CIRs in factories at 1.3 GHz [49], [50], and from outdoor cellular channel PDPs [51], [52]. These CIR models were popular with industry in the early years of digital cellular and WiFi [53]. The SIRCIM and SMRCIM models were based on statistical and geometrical models to synthesize the phases and directions of arrival and departure in an IR model [53], [54].

6) *Kronecker Model*: The MIMO channel covariance matrix can be decomposed into the Kronecker product of the transmit and receive covariance matrices, and the corresponding CIRs for a MIMO system can be computed using the high-order single-value decomposition (SVD) method [55]. This method was shown to improve accuracy in predicting channel capacities in the UHF and microwave spectrum [56].

## II. WIDEBAND PROPAGATION MEASUREMENTS

### A. Measurement System Description

A 400-megachips-per-second (Mcps) broadband sliding correlator channel sounder was used to measure the 28- and 73-GHz wideband urban channel over a 800-MHz null-to-null RF bandwidth, where the RX locations were placed on New York City streets and inside one building with T-R separation distances ranging from 20 to 425 m. Recorded outages over all measured RX locations are given in [31] and [38], and can be used to determine the conditional probability of a link being made when using a CIR. The transmitter output power was varied between 11 dBm (for close, LOS receiver locations) up to a maximum of 14.6 dBm at 73 GHz and 30 dBm at 28 GHz (for the NLOS locations). A pair of steerable (rotatable) directional horn antennas of 24.5 dBi, with 10.9° and 8.6° HPBWs in the azimuth and elevation planes, respectively (used at 28 GHz) and 27 dBi, with 7° HPBW in both azimuth and elevation, respectively (used at 73 GHz) were used to perform TX and RX azimuth antenna sweeps at various fixed TX/RX elevation pointing angles for each location, with static PDPs measured in azimuth step increments equal to one HPBW (10° or 7° at 28 and 73 GHz, respectively). Additional channel sounder specifications used during the propagation measurements in New York City can be found in Table I and [11], [57], [58]. Fig. 1 shows a photo of the 73-GHz transmitter used during the measurements.

Independent frequency sources at the TX and RX were used in the 28- and 73-GHz channel sounder to provide the

TABLE I  
BROADBAND SLIDING CORRELATOR CHANNEL SOUNDER  
SPECIFICATIONS USED IN THE 28- AND 73-GHz  
NEW YORK CITY MEASUREMENTS [11], [12], [57]

Parameter	Value	
	28 GHz	73 GHz
RF Bandwidth (Null-to-Null)	800 MHz	
Sequence	11 <sup>th</sup> Order PN Code (Length = 2047)	
Transmitter Chip Rate	400 Mcps	
Receiver Chip Rate	399.95 Mcps	
Slide Factor	8,000	
Multipath Time Resolution	2.5 ns	
NI Digitizer Sampling Rate	2 MSamples/s	
TX Maximum Output Power	30.1 dBm	14.6 dBm
TX-RX Antenna Gains	24.5 dBi	27 dBi
TX-RX Antenna 3 dB Beamwidths (Az./El.)	10.9° / 8.6°	7° / 7°
Maximum Measurable Path Loss (5 dB SNR)	178 dB	181 dB



Fig. 1. Photo of the 73-GHz transmitter used during the New York City measurements.

PN clocks, and the intermediate frequency, and we note that the local oscillator signals on both TX and RX were not phase-synchronized, causing a lack of absolute time stamping.

Observed jitter was removed with additional LabVIEW post-processing software designed to provide a real-time trigger alignment of the *I* and *Q* waveforms, in which 20 successive PDPs at one measured angle were aligned to the time of arrival of the strongest received multipath component before averaging. The PDPs collected at unique pointing angle directions provided excess time delay PDPs, relative to the first arriving multipath component. Complementary 3-D ray-tracing software was developed to recreate the absolute propagation time of multipath arrivals from TX to RX [40].

### B. Measurement Procedure Description

12 000 wideband PDPs were recorded at 28 and 73 GHz in New York City using a 400-Mcps broadband sliding correlator channel sounder and directional steerable horn antennas to recover AOD and AOA statistics. The directional steerable horn antennas were exhaustively rotated in the azimuth and elevation planes, and many thousands of PDPs were collected at distinct azimuth and elevation unique pointing angles at 26 RX and 74 RX outdoor locations at 28 and 73 GHz, respectively.

For the 28-GHz measurements, the RX antenna was rotated in the azimuth plane in step increments of 10° (one HPBW), at RX elevation planes of +/- 20° and 0° for a fixed TX azimuth/elevation pointing angle to emulate a practical cellular deployment scenario where BS antennas are usually downtilted toward the street to provide maximum covered street areas. This procedure was repeated for three distinct TX azimuth angles, resulting in a total of nine RX azimuth sweeps. One additional TX azimuth sweep was performed at a fixed -10° downtilt, and for a fixed RX azimuth/elevation pointing angle, where the TX antenna was rotated in azimuthal step increments of 10°. A PDP was acquired at each TX-RX unique pointing angle. A similar procedure was performed for the 73-GHz measurements, where the RX elevation planes were adjusted in 7° step increments, in real time during the field measurements, based on the strongest measured elevation plane (elevation plane with strongest received power). Many thousands of unique TX-RX pointing angle PDPs were measured, thereby capturing the majority of significant and most powerful multipath components to extract accurate path loss and multipath properties. Additional details of the measurement campaigns can be obtained in [12].

### III. SYNTHESIZING OMNI PDPs FROM MEASUREMENTS

A 3-D MATLAB-based ray-tracer was developed to recover absolute propagation time delays of the PDP measurements. The downtown Manhattan environment was modeled in Google SketchUp over an 800 × 800 m<sup>2</sup> area, which allowed fast and easy 3-D site-specific modeling using simple geometrical shapes such as cubes. The 3-D information was then exported in XML format, and subsequently extracted to numerically reconstruct and discretize the environment in MATLAB [35].

Fig. 2 shows a typical ray-traced map where each ray that leaves the TX and successfully arrives at the RX is depicted for a measured TX-RX location pair. The predicted AOAs are

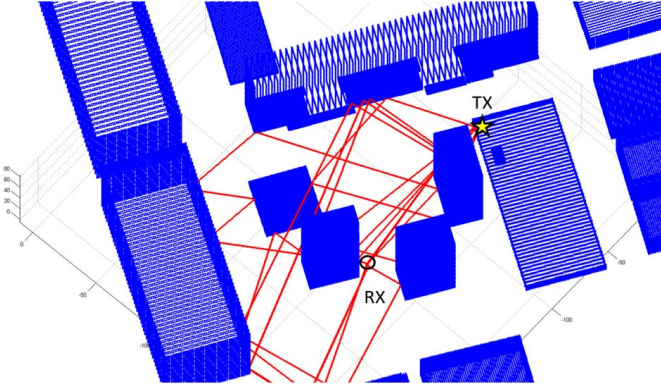


Fig. 2. 3-D view of the downtown Manhattan area. The rays shown in red leave the TX and successfully arrive at the RX, and represent viable multipath signal propagation paths [38].

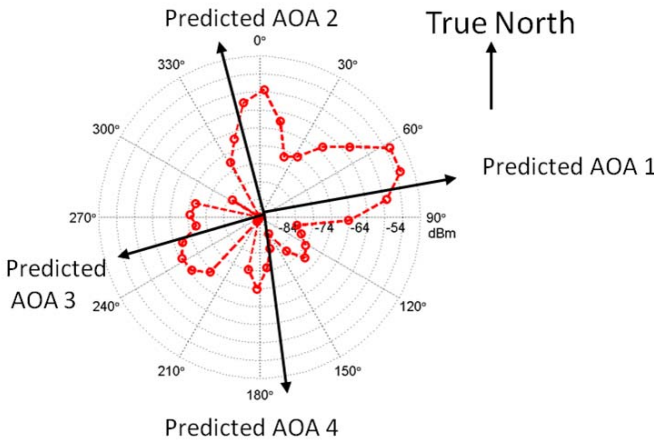


Fig. 3. Azimuthal distribution of total received power (dBm units), also referred to as polar plot, showing the predicted 28-GHz AOAs using 3-D ray-tracing at the Manhattan RX location on Wooster Street [11].

shown in Fig. 3, denoted with black arrows on top of the 28-GHz measured power azimuth spectrum for that RX location. The ray-tracer predicted the strongest AODs and AOAs with an accuracy of  $\pm 20^\circ$  (i.e.,  $\pm 2$  antenna beamwidths), which provided sufficient accuracy to pair the strongest PDPs with the estimated absolute propagation delay at the predicted angles.

Figs. 4–7 show the 28-GHz excess delay PDPs corresponding to the strongest measured azimuth AOAs at a  $0^\circ$  RX elevation, found by searching  $\pm 2$  antenna beamwidths about the predicted azimuth AOAs. The absolute propagation times, as computed from the ray-tracing software, are shown at the bottom of the four figures, and were used to properly time-shift each PDP appropriately over an absolute propagation time axis, to synthesize the equivalent omnidirectional PDP as would have been measured with an omnidirectional antenna with comparable gain of the horns.

The resulting omnidirectional PDP is shown in Fig. 8, where each excess delay PDP was appropriately time-shifted using the absolute propagation time (obtained by dividing the ray-traced propagation distance by the speed of light) of the first arriving peak at the corresponding RX azimuth angle. In Figs. 4–7, the absolute propagation times of the

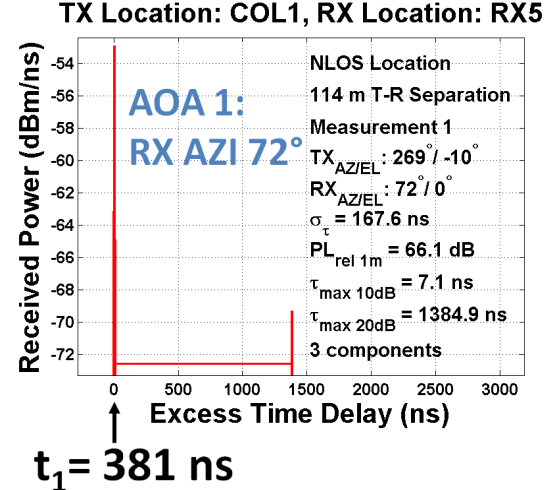


Fig. 4. PDP measured at an RX azimuth/elevation of  $72^\circ/0^\circ$  and a TX azimuth/elevation of  $269^\circ/-10^\circ$ , and predicted by the 3-D ray-tracer. Azimuth angles are with respect to a True North  $0^\circ$  angle.

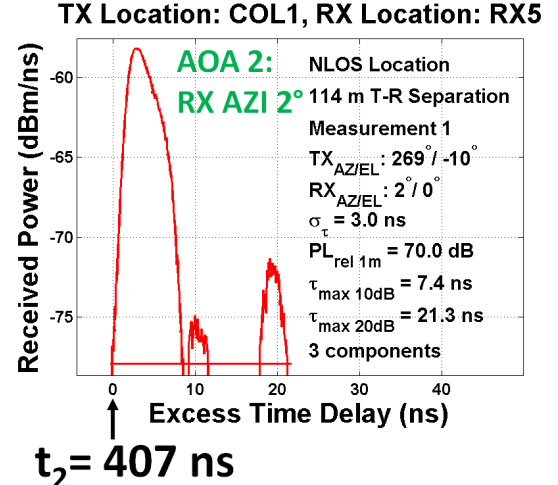


Fig. 5. PDP measured at an RX azimuth/elevation of  $2^\circ/0^\circ$  and a TX azimuth/elevation of  $269^\circ/-10^\circ$ , and predicted by the 3-D ray-tracer. Azimuth angles are with respect to a True North  $0^\circ$  angle.

first arriving peak for AOA 1, 2, 3, and 4 are 381, 407, 1433, and 1500 ns, respectively. Since the four angles are orthogonal without beam overlap, the four excess delay PDPs were shifted and summed in mW/ns to synthesize omnidirectional PDPs. This example showed the method for superimposing PDPs over the RX azimuth plane. The PDPs from strongest TX and RX angles were summed over the azimuth and elevation dimensions, yielding 3-D omnidirectional PDPs with absolute timing. Due to database or antenna pointing errors at some locations, we created omnidirectional PDPs for 3 of 6 measured LOS locations and 13 of 20 measured NLOS locations at 28 GHz, and for 5 of 5 measured LOS locations and 19 out of 25 measured NLOS locations at 73 GHz, using the few strongest predicted AODs and AOAs. The synthesized absolute timing omnidirectional PDPs are obtained from the strongest measured TX and RX pointing angles, which capture strong multipath components traveling in the channel,

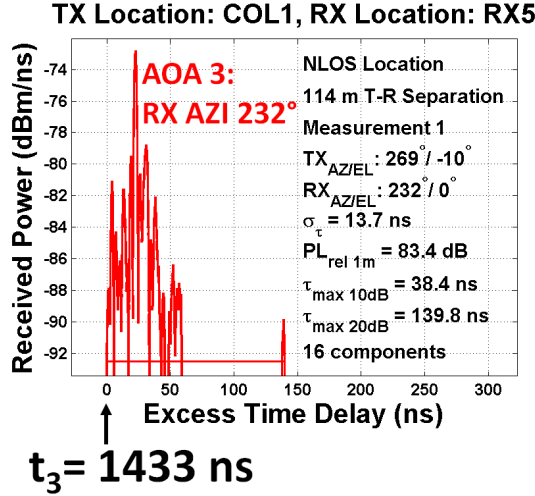


Fig. 6. PDP measured at an RX azimuth/elevation of 232°/0° and a TX azimuth/elevation of 269°/-10°, and predicted by the 3-D ray-tracer. Azimuth angles are with respect to a True North 0° angle.

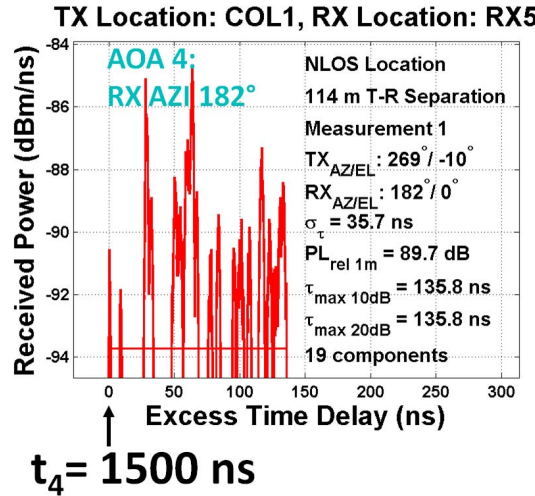


Fig. 7. PDP measured at an RX azimuth/elevation of 182°/0° and a TX azimuth/elevation of 269°/-10°, and predicted by the 3-D ray-tracer. Azimuth angles are with respect to a True North 0° angle.

in addition to weaker multipaths as a result of significant local scattering in the environment, to provide realistic omnidirectional channel models. This SSCM provides a realistic and comprehensive model that is capable of modeling the statistics of both strong and weak multipath components.

#### A. Omnidirectional LOS and NLOS Path Loss Models

Omnidirectional path loss models are necessary to estimate the total received power for arbitrary distance and antenna pattern (see Step 2 in Section IV-A). Omnidirectional path losses were found by summing the received powers measured at each unique non-overlapping azimuth and elevation antenna pointing angle and recovering the path losses after carefully removing double counts (arising from TX and RX sweeps) and antenna gains [59]. This procedure is valid since adjacent angular beamwidths are orthogonal to each other, and the phases of arriving multipath components with such short

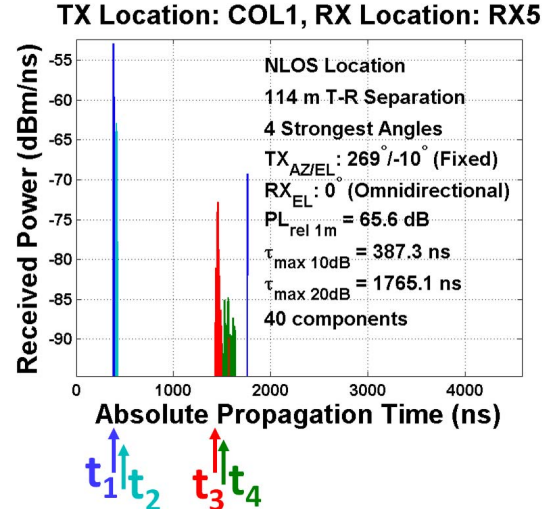


Fig. 8. Omnidirectional PDP synthesized using the 3-D ray-tracing absolute time of arrivals and the four excess delay PDPs shown in Figs. 4–7, at TX location Coles 1 (COL1).

wavelengths with different propagation paths are identically and independently distributed (i.i.d.) and uniform between 0 and  $2\pi$ , such that powers may be added [10], [12], [60]

$$Pr_{\text{Ommi}} = \sum_{i,j} \sum_{k,m} Pr(\theta_{TX,i}, \phi_{TX,j}, \theta_{RX,k}, \phi_{RX,m})(d) \quad (1)$$

$$PL[\text{dB}](d) = P_{\text{TX}} + G_t + G_r - 10 \times \log_{10}(Pr_{\text{Ommi}}) \quad (2)$$

$$PL[\text{dB}](d) = PL_{\text{FS}}(d_0) + 10\bar{n} \log_{10}\left(\frac{d}{d_0}\right) + \chi_\sigma \quad (3)$$

where  $i, j, k$ , and  $m$  are indices denoting unique pointing directions in azimuth and elevation at the TX and RX, respectively,  $(\theta_{TX}, \phi_{TX}, \theta_{RX}, \phi_{RX})$  denote the TX azimuth and elevation angles, and the RX azimuth and elevation angles, respectively,  $P_{\text{TX}}$  is the transmit power in dBm,  $G_t$  and  $G_r$  are the TX and RX horn antenna gains in dBi, respectively,  $PL_{\text{FS}}(d_0)$  is the frequency-dependent free space path loss at distance  $d_0$ ,  $\bar{n}$  is the average PLE over distance,  $\lambda$  is the carrier wavelength, and  $\chi_\sigma$  is a zero-mean lognormal random variable with standard deviation  $\sigma$  modeling large-scale signal fluctuations.

The antenna de-embedding was performed by removing the antenna boresight gain from every measured PDP at each and every TX-RX antenna pointing angle. In the measurements, the horn antennas were incremented in steps of one HPBW in the azimuth plane, thereby minimizing overlapping effects of two adjacent radiation patterns. When considering the equivalent omnidirectional antenna pattern arising from the aggregation of adjacent beamwidths, the effective omnidirectional antenna pattern has a relatively constant gain, as shown in [60, Fig. 1]. The antenna cross-polarization ratios (XPRs) were 21 and 25.4 dB for the 28- and 73-GHz outdoor measurements [61], indicating a minor and negligible impact of cross-polar contributions. Note that impact of antenna sidelobes was also minor, with sidelobe levels  $-20$  dB below boresight gain when beyond one HPBW.

The  $d_0 = 1$  m CI free space reference distance path loss model is a much simpler path loss model than the

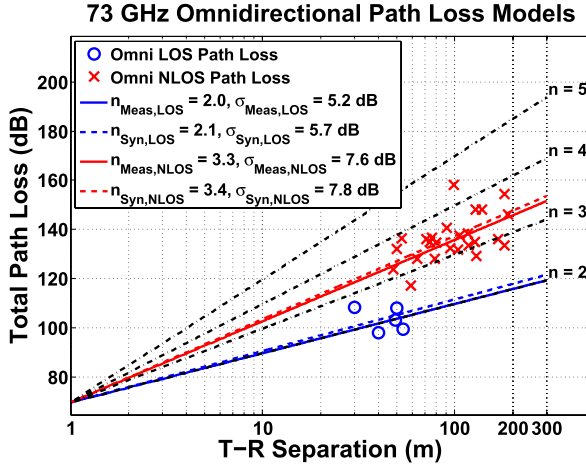


Fig. 9. 73 GHz (mobile) omnidirectional path loss models for the LOS and NLOS environments, obtained from the wideband measurements in Manhattan. The omnidirectional power at each RX location was obtained from all PDPs for all RX and TX pointing angles (and removing double-counted angles), and antenna gains were removed from each PDP.

3GPP/WINNER least-squares best fit regression line (named floating-intercept model, or FI for short). The current 3GPP/WINNER path loss models use two parameters to describe path loss over distance (a slope and an intercept), which are highly dependent upon the number of path loss samples measured and corresponding distances. The CI model, however, uses just one parameter, the PLE, making it more stable across various path loss data sets, frequencies, and environments [12], [27], [33], [62], while remaining steeped in physics to a physical free space path loss value at a distance of 1 m, which can always be considered to be within LOS of a BS. Using the CI model, it is therefore easier to compare path loss results from different research groups. Further, the CI model can be used as a global standard for comparing path loss models across different frequencies or scenarios [12], [27], [33]. The CI and FI models have been shown to perform similarly over identical data sets, with standard deviation errors within a fraction of a decibel [12], [27], [63]. Similarly, when considering a probabilistic path loss model used in system-level simulations, which takes into account the probability of LOS, there is virtually no difference between the CI and FI models [35].

Fig. 9 shows the omnidirectional path losses from the 73 GHz LOS and NLOS measurements, computed from (1) and (2), and corresponding path loss parameters using a  $d_0 = 1$  m CI free space reference distance in (3). Using (3), the omnidirectional PLE and shadow factor (SF) in LOS were  $\bar{n}_{\text{LOS}} = 2.0$  and  $\sigma_{\text{LOS}} = 5.2$  dB, matching free space propagation ( $n = 2$ ). In NLOS, we obtained  $\bar{n}_{\text{NLOS}} = 3.3$  and  $\sigma_{\text{NLOS}} = 7.6$  dB, showing greater attenuation over distance due to obstructions. To verify the method shown in (8), we also computed the path loss parameters from the synthesized absolute timing PDPs, yielding  $\bar{n}_{\text{Syn}} = 2.1$  and  $\sigma_{\text{Syn}} = 5.7$  dB, and  $\bar{n}_{\text{Syn}} = 3.3$  and  $\sigma_{\text{Syn}} = 7.8$  dB in LOS and NLOS, respectively, in agreement with the measured data. This indicates that only a few of the strongest AODs and AOAs (up to four such angles) are sufficient to recover an accurate

path loss channel model. Similar results were obtained for the 28-GHz data set [40].

#### IV. JOINT TEMPORAL-SPATIAL mmWAVE CIR

The radio propagation channel is commonly represented by the superposition of many plane waves, and is parameterized with the double-directional CIR [64]. The omnidirectional CIR  $h_{\text{omni}}(t, \vec{\Theta}, \vec{\Phi})$  is expressed as [38]

$$h_{\text{omni}}(t, \vec{\Theta}, \vec{\Phi}) = \sum_{n=1}^N \sum_{m=1}^{M_n} a_{m,n} e^{j\varphi_{m,n}} \cdot \delta(t - \tau_{m,n}) \cdot \delta(\vec{\Theta} - \vec{\Theta}_{m,n}) \cdot \delta(\vec{\Phi} - \vec{\Phi}_{m,n}) \quad (4)$$

where  $t$  denotes absolute propagation time,  $\vec{\Theta} = (\theta, \phi)_{\text{TX}}$  is the vector of azimuth and elevation AODs, and  $\vec{\Phi} = (\theta, \phi)_{\text{RX}}$  is the vector of azimuth and elevation AOAs;  $N$  and  $M_n$  denote the number of TCs (also defined in Section IV-A) and the number of cluster **subpaths** (SPs), respectively;  $a_{m,n}$  is the magnitude of the  $m$ th SP belonging to the  $n$ th TC;  $\varphi_{m,n}$  and  $\tau_{m,n}$  are the phases and propagation time delays, respectively;  $\vec{\Theta}_{m,n}$  and  $\vec{\Phi}_{m,n}$  are the azimuth/elevation AODs and azimuth/elevation AOAs, respectively, of each multipath component. Note that a SP is an individual multipath component contained in either a SL or TC.

The omnidirectional CIR can further be partitioned to yield *directional* PDPs at a desired TX-RX unique antenna pointing angle, and for arbitrary TX and RX antenna patterns [16]

$$h_{\text{dir}}(t, \vec{\Theta}_d, \vec{\Phi}_d) = \sum_{n=1}^N \sum_{m=1}^{M_n} a_{m,n} e^{j\varphi_{m,n}} \cdot \delta(t - \tau_{m,n}) \cdot g_{\text{TX}}(\vec{\Theta}_d - \vec{\Theta}_{m,n}) \cdot g_{\text{RX}}(\vec{\Phi}_d - \vec{\Phi}_{m,n}) \quad (5)$$

where  $(\vec{\Theta}_d, \vec{\Phi}_d)$  are the desired TX-RX antenna pointing angle,  $g_{\text{TX}}(\vec{\Theta})$  and  $g_{\text{RX}}(\vec{\Phi})$  are the arbitrary 3-D (azimuth and elevation) TX and RX complex amplitude antenna patterns of multi-element antenna arrays, respectively. In (5), the TX and RX antenna patterns amplify the power levels of all multipath components lying close to the desired pointing direction, while effectively setting the power levels of multipath components lying far away from the desired pointing direction to 0.

The statistical channel model also produces the joint AOD-AOA power spectra  $P(\vec{\Theta}, \vec{\Phi})$  in 3-D obtained by integrating the magnitude squared of (4) over the propagation time dimension,

$$P(\vec{\Theta}, \vec{\Phi}) = \int_0^\infty |h_{\text{omni}}(t, \vec{\Theta}, \vec{\Phi})|^2 dt \quad (6)$$

$$P(\vec{\Theta}, \vec{\Phi}) = \sum_{n=1}^N \sum_{m=1}^{M_n} |a_{m,n}|^2 \cdot \delta(\vec{\Theta} - \vec{\Theta}_{m,n}) \cdot \delta(\vec{\Phi} - \vec{\Phi}_{m,n}). \quad (7)$$

Previous work modeled the CIR as a function of time [65], azimuth AOA [66], [67], and both AOD and AOA azimuth/elevation angles [42]. Note, however, that [42] models AOD and AOA azimuth and elevation information for the

in-building, indoor-to-outdoor, and outdoor-to-indoor scenarios, but only azimuth, and not elevation, for the microcellular environment. Here, each multipath component of the IR model is assigned a unique combination of AOD and AOA azimuth and elevation angles based on measured data to simulate realistic outdoor mmWave channels. This modeling approach supports use of directionality at both the BS and mobile handsets [68].

### A. Time Clusters and Spatial Lobes Statistics

The SSCM given here uses TCs and SLs to model the omnidirectional CIR and corresponding joint AOD-AOA power spectra, which have been used successfully in modeling mmWave channels [38], [40]. **TCs** are composed of multipath components traveling close in time, and that arrive from potentially different directions in a short propagation time window. **SLs** represent main directions of arrival (or departure) where energy arrives over several hundred nanoseconds. This SSCM structure is motivated by field measurements [11], [57] which have shown that multiple TCs can arrive at unique pointing angles, detectable due to high gain directional antennas, and this feature has not been modeled in current 3GPP and WINNER models. These definitions decouple the time and space dimensions by extracting temporal and spatial statistics separately. The definition of TC here considers multipath components traveling close in time, but that can arrive from many lobe angular directions, whereas current 3GPP and WINNER models assume that SPs belonging to a cluster travel along the same propagation path, but arrive at the *same* time delay over a certain AOA angular spread.

The TCSL approach implements a physically based clustering scheme (e.g., the use of a fixed inter-cluster void interval representing the minimum propagation time between likely reflection or scattering objects) derived from field observations, and can be used to extract TC and SL statistics for any ray-tracing or measurement data sets. Note the channel models provided in [40] are 2.5-D and are valid for omnidirectional azimuth planes using unique elevation planes or pointing angles, while the models provided in [16] and [38] and in this paper describe true 3-D azimuth and elevation channels where the TCSL framework models the directionality of the channels through separate TCs that have time-delay statistics, and through SLs which represent the strongest directions of multipath arrival and departure [15]–[17], [38], [40], [69]. The approach used here is an extension of early work where intra-cluster SPs with *distinct* delays were successfully used in modeling the indoor environment based on wideband channel measurements [65], [66].

MmWave CIRs and power angular spectra can be partitioned conveniently using the definitions of TCs and SLs, respectively. Fig. 10 shows a typical received omnidirectional PDP at 28 GHz. The time-partitioning methodology is shown in Fig. 10 by delineating the beginning and end times of each TC, using a 25-ns minimum inter-cluster void interval. Sequentially arriving multipath components that occur within 25 ns of each other are assumed to belong to one TC. In defining Fig. 10, two TCs are composed of 8 and 6 SP components with random delays, amplitudes, and AOAs. True

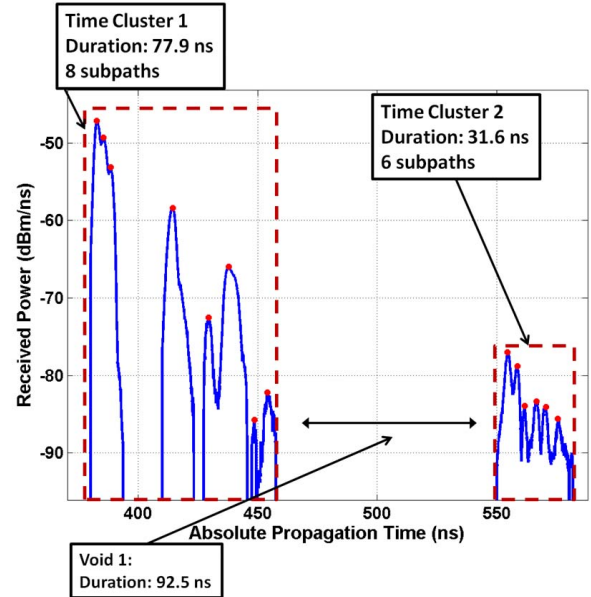


Fig. 10. Typical measured omnidirectional PDP, where two TCs are composed of eight and six SP components, assuming a 25-ns minimum inter-cluster void interval. Using a peak detection algorithm, the SP components are found to have randomly varying AOAs, delays, and amplitudes [10], [16], [40].

to real-world measurements, the total power in one TC is also random, as it is composed of the sum of randomly varying SP powers. In addition, the propagation phases of each multipath component can be taken to be i.i.d. uniform between 0 and  $2\pi$  [65]. By counting the number of TCs and intra-cluster SPs, and extracting TC and SP delays and power levels from all available measured PDPs, measurement-based statistical distributions are obtained and allow reconstruction of time-varying IRs that embody the statistics of the collected data. The key parameters for generating mmWave PDPs are the number of TCs, the number of intra-cluster SPs, the TC and SP delays, and the TC and SP power levels [38], [40].

Since directional transmissions will play a role in mmWave communications, it is equally important to characterize the spatial angular channel at the transmitter and at the receiver. Fig. 11 shows a typical measured power azimuth spectrum obtained with a horn antenna in an NLOS environment, where each dot corresponds to the total received power (area under PDP) measured at azimuth angles in step increments of  $10^\circ$ . Fig. 11 illustrates the concept of SLs, by showing that energy arrives at distinct mean pointing AOAs over a contiguous range of azimuth angles and a  $-10$ -dB power threshold with respect to the maximum received angle power. While five mean pointing AOAs can be identified in Fig. 11 at azimuth angles of  $65^\circ$ ,  $0^\circ$ ,  $240^\circ$ ,  $180^\circ$ , and  $130^\circ$  with greatly varying powers, it is sufficient in practice to keep track of the few strongest mean pointing SL AOAs by defining a  $-10$ - or  $-20$ -dB power threshold with respect to the maximum peak power in the 3-D spectrum in LOS and NLOS, below which all power levels can be disregarded. Note that we had previously used  $-10$ - and  $-20$ -dB thresholds in LOS and NLOS environments when considering 2-D polar plots [40]. Polar plots can be easily reconstructed having knowledge of the number of SLs, the mean pointing AOAs, the lobe ASs,

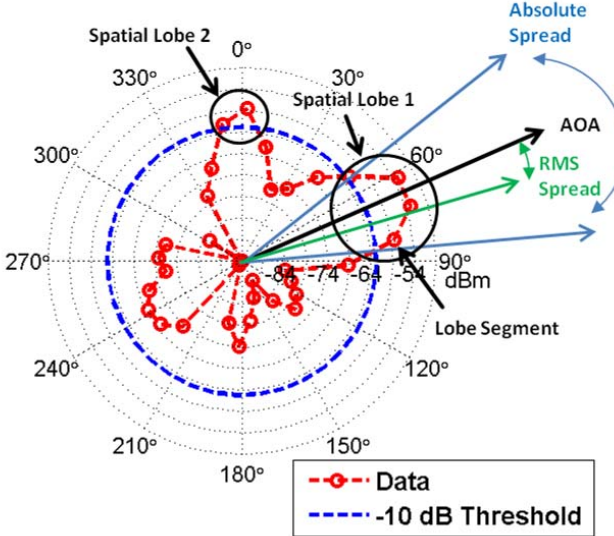


Fig. 11. Measured power azimuth spectrum, also called polar plot, showing a  $-10$ -dB power threshold and two SLs, where the threshold is with respect to the maximum received angle power. An SL has well-defined properties such as its mean pointing angle, its absolute angle spread, and its RMS angle spread [10], [16], [40].

and the RMS lobe AAs. While this example shows a 2-D polar plot, the work presented here uses 3-D power angular spectra that also include the elevation dimension.

To benchmark the accuracy of the resulting SSCM model and simulator against real data, we define key parameters, or *primary statistics*, as measurement-based statistical distributions used to generate mmWave temporal and spatial channel parameters for a time-varying IR. A good test procedure for checking the accuracy of the channel model can be devised by not just comparing first-order statistics, but by also looking at second-order statistics, or *secondary statistics*, of the generated IRs, such as the RMS DSs and RMS lobe angular spreads.

### B. Time Cluster Partitioning

The TC partitioning scheme heavily affects the outcome of the temporal channel parameter statistics. In this work, a 25-ns minimum *inter-cluster void interval* was defined to segment omnidirectional PDPs based on time of arrivals, where consecutive multipath components that occur within a time duration less than 25 ns were assumed to belong to one TC. This simple clustering scheme allows us to resolve intricate multipath channel dynamics within the smallest multipath time resolution offered by the 3GPP and WINNER models (20 ns) [41], [42], and is easily adjustable to resolve temporal statistics over arbitrary time resolutions using a different minimum inter-cluster void interval. The value of 25 ns for the minimum inter-cluster void interval was found to match the measured data, and makes sense from a physical standpoint, since multipath components tend to arrive in clusters at different time delays over many angular directions, most likely due to the free space air gaps between reflectors (buildings, lampposts, streets). The narrowest streets have a typical width of 8 m (25 ns in propagation delay) in New York City, thus

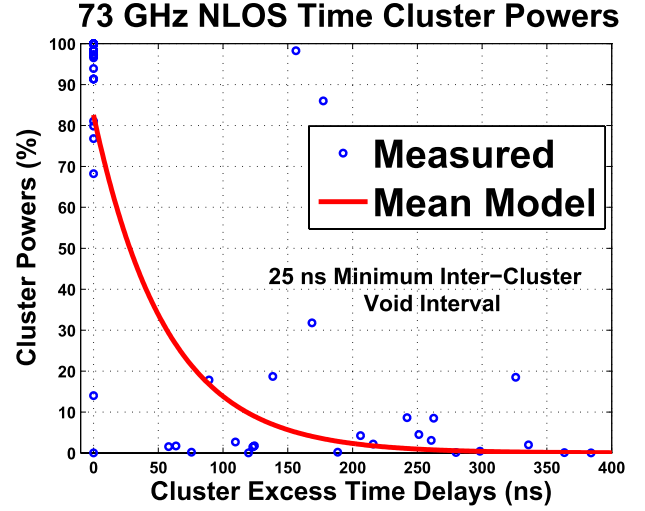


Fig. 12. Cluster powers extracted from 73-GHz NLOS omnidirectional PDPs using a 25-ns minimum intercluster void interval, with decay time constant  $\Gamma = 56.0$  ns and y-intercept  $\bar{P}_0 = 0.826$ .

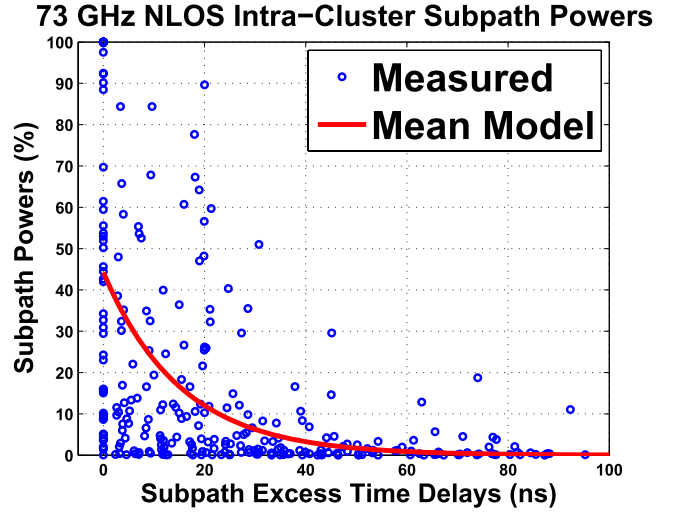


Fig. 13. Intra-cluster SP powers extracted from 73-GHz NLOS omnidirectional PDPs using a 25-ns minimum inter-cluster void interval, with decay time constant  $\gamma = 15.4$  ns and y-intercept  $\bar{P}_0 = 0.442$ .

physically describing the regularly observed minimum void interval for arriving energy.

Fig. 12 shows the 73-GHz NLOS cluster power levels, normalized to the total received power, as a function of cluster excess delays, extracted from absolute timing omnidirectional PDPs using a 25-ns minimum inter-cluster void interval. The mean exponential model, found using a least-squares regression, is parameterized using the cluster decay time constant  $\Gamma$ , defined as the excess time delay when average cluster power falls to  $37\%$  ( $1/e$ ), and the y-intercept at  $\tau = 0$  ns, which physically represents the average power  $\bar{P}_0$  contained in the first arriving TC. Here, we found  $\Gamma = 56.0$  ns and  $\bar{P}_0 = 0.826$ . It is worth noticing in Fig. 12 that the large cluster power levels for two measurement locations at  $\tau = 156$  ns and  $\tau = 177$  ns are carrying  $98\%$  and  $86\%$  of the total received power for those PDPs, respectively, and this situation causes large RMS DSs. Fig. 13 shows the

TABLE II

KEY TC AND SL MODEL PARAMETERS NECESSARY TO GENERATE mmWave 3-D CIRs [16], [17]. THE MODELING STEP PROCEDURES AND DISTRIBUTION MEANS AND STANDARD DEVIATIONS ARE PROVIDED IN SECTION V-A AND TABLE IV

TC / SL	Symbol	Name of Parameter	Distribution	Step #
TC	$N$	Number of Time Clusters	Discrete Uniform [1, 6]	Step 3
	$M_n$	Number of Subpaths	Discrete Uniform [1, 30]	Step 4
	$\tau_n, P_n$	Cluster Delays, Powers	Exponential, Lognormal	Steps 6 & 7
	$\rho_{m,n}, \Pi_{m,n}$	Subpath Delays, Powers	Exponential, Lognormal	Steps 5 & 8
	$\varphi_{m,n}$	Subpath Phases	Uniform (0, $2\pi$ )	Step 9
SL	$L$	Number of Spatial Lobes (AOD & AOA)	Poisson	Step 3
	$\theta, \phi$	Lobe Az./El. Angles (AOD & AOA)	Uniform (0, 360), Gaussian	Step 11
	$\sigma_\theta, \sigma_\phi$	RMS Lobe Az./El. Spreads (AOD & AOA)	Gaussian, Laplacian	Step 12

73-GHz NLOS intra-cluster SP power levels (normalized to the TC power), and the corresponding mean exponential curve model. The curve is parameterized with  $\gamma = 15.4$  ns and  $\bar{P}_0 = 0.442$ . The smaller  $\gamma$  physically denotes that intra-cluster SP components decay much faster than TCs. Note that similar plots were shown in [38, Figs. 3 and 4] for the 28-GHz NLOS case, with measured cluster and SP decay time constants of  $\Gamma = 49.4$  ns and  $\gamma = 16.9$  ns, which are similar to the 73-GHz NLOS time constants, indicating little dependence upon carrier frequency. When combining the 28- and 73-GHz LOS cluster and SP power levels, we found  $\Gamma = 25.9$  ns and  $\gamma = 16.9$  ns, showing that cluster powers decay much faster in LOS than in NLOS environments. Table IV summarizes the  $\Gamma$ 's and  $\gamma$ 's as a function of environment and carrier frequency.

The choice of the minimum inter-cluster void interval can significantly impact the cluster and SP power levels. While a 25-ns minimum inter-cluster void interval worked well for generating PDPs whose RMS DSs match with measured data, we also investigated the temporal statistics under 2.5- and 20-ns minimum inter-cluster void intervals, which yielded  $\Gamma = 24.4$  ns and  $\Gamma = 29.9$  ns, respectively, for the 73-GHz NLOS scenario, compared with  $\Gamma = 56.0$  ns when using a 25-ns inter-cluster void interval. The  $\Gamma$ 's can vary greatly for different minimum inter-cluster void intervals. As the minimum inter-cluster void interval increases, the number of TCs in a given PDP must decrease, while the number of intra-cluster SPs must increase, and consequently, the cluster powers must increase yielding a larger  $\Gamma$ , and the intra-cluster SP powers must decrease yielding a smaller  $\gamma$ . For minimum inter-cluster void intervals of 2.5 and 20 ns, there are many more cluster power levels carrying very little power that shift the mean exponential model curve downward, with the resulting omnidirectional RMS DSs of the simulated PDPs much smaller than the measured data. Table II summarizes the TC model parameters.

### C. 3-D Spatial Lobe Thresholding

The 3-D spatial distribution of received power was reconstructed from the 28- and 73-GHz LOS and NLOS directional received powers by linearly interpolating adjacent power level

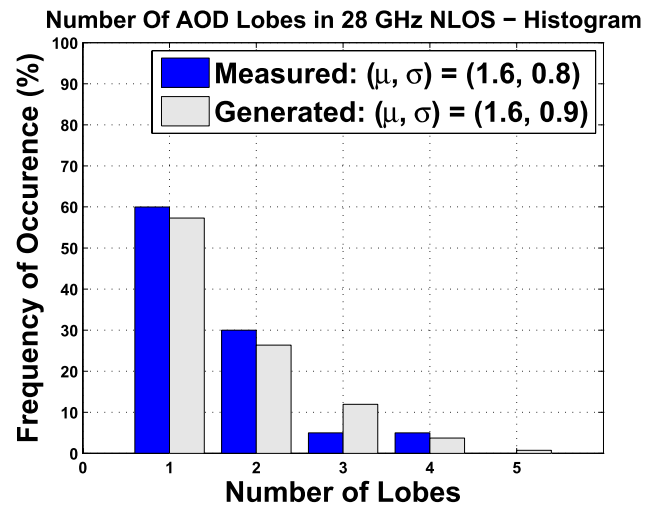


Fig. 14. Measured number of AOD lobes extracted from 28-GHz power azimuth spectra, using a  $-10$ -dB threshold, with a mean and a standard deviation of 1.6 and 0.8, respectively. The simulated distribution is a Poisson distribution with a mean of 1.8 (see Step 3 in Section V-A).

segments in azimuth and elevation with a  $1^\circ$  resolution and extracting 3-D spatial angular statistics. We used a  $-10$ -dB threshold below maximum peak power in the 3-D power spectrum in both LOS and NLOS environments, where all power segments below this threshold were disregarded for further processing. Note that work shown in [15] and [40] sometimes used a  $-20$ -dB threshold, but here we use a  $-10$ -dB lobe threshold to remain consistent.

Fig. 14 shows a typical empirical histogram plot of the number of AOD SLs extracted from 28-GHz NLOS power angular spectra, next to the simulated histograms as explained in Step 3 of Section V, yielding good agreement with the measured distributions. The mean numbers of AOD and AOA SLs were both 1.6 for the 28-GHz NLOS measurements, and 1.5 and 2.5, respectively, for the 73-GHz NLOS measurements, showing very little dependence on carrier frequency from the BS perspective. However, there are more AOA SLs found at 73 GHz, most likely arising from more prominent local scattering than at 28 GHz. In the 28–73-GHz combined LOS scenario, the mean number of AOD lobes

was 1.9, compared with 1.5 and 1.6 in the NLOS case at 28 and 73 GHz, respectively, showing that multipath signals can reach the RX from more departing directions. The mean number of AOA SLs was 1.8 in the combined 28–73-GHz LOS scenario, which is comparable to the mean number of AOA SLs found in the combined 28–73-GHz NLOS scenario, suggesting that LOS and NLOS spatial environments appear similar to a receiver. SL statistics are summarized in Table IV as a function of environment and frequency. Table II summarizes the SL model parameters.

## V. GENERATING TEMPORAL AND SPATIAL CHANNEL PARAMETERS

This section outlines the step procedure for generating 3-D mmWave temporal and spatial channel parameters in (4) and (5), e.g., for producing sample functions for an SSCM, in both LOS and NLOS, generalized to arbitrary carrier frequency, signal bandwidth, and antenna beamwidth [16] by closely following the 3GPP model [41]. The SSCM reproduces the omnidirectional CIR between a single TX and single RX antennas, or single input single output (SISO), by separately modeling the temporal and spatial statistics. The omnidirectional CIR for SISO system can readily be extended to a local area using knowledge of small-scale spatial amplitudes and spatial autocorrelations of the multipath amplitudes over tens of wavelengths to emulate a true MIMO communication link [69], [70]. In Step 12, the SP components are randomly assigned to the SL AODs and AOAs in a uniform random fashion, thereby recoupling time and space to produce an accurate joint spatio-temporal SSCM, while remaining faithful to our definitions of TC and SL. The 3-D SSCM is based on measurements in [11] and [57] and is valid for any noise floor greater than  $-100$  dBm (over an 800-MHz RF bandwidth), or any total link dynamic range less than 180 dB, and for RF bandwidths less than 800 MHz and antennas with beamwidths greater than  $7^\circ$ . The model can be used for bit-error simulations as was done in first-generation digital cellular [71].

The 73-GHz SCM in [34] uses the 3GPP delay-angle cluster, where a cluster corresponds to a group of multipath components with similar propagation delays, AODs, and AOAs. The model parameters are obtained in [32] and [34] making a blind assumption that the 3GPP model framework used for sub-6-GHz channel models represents mmWave channels. The step procedures below generalize the 3GPP delay-angle cluster approach by using the concepts of TCSL approach, which considers the time and angle dimensions separately. The TCSL modeling approach was shown to accurately recreate the measured global and directional RMS delay and angular spreads statistics [16].

In the following steps,  $DU$  corresponds to the *discrete uniform* distribution, and the notation  $[x]$  denotes the closest integer to  $x$ . Steps 11 and 12 apply to both AOD and AOA SLs.

### A. Step Procedure for Generating Channel Coefficients

*Step 1: Generate the TX-RX separation distance  $d$  (in 3-D) ranging from 30 to 60 m in LOS and from*

TABLE III  
MEASURED PLES AND SHADOW FACTORS [12], [59] USED TO GENERATE THE OMNIDIRECTIONAL RECEIVED POWER IN STEP 2 OF SECTION V-A

Step #	Frequency	Environment	Measured( $\bar{n}, \sigma$ )
Step 2	28 GHz	LOS	(2.1, 3.6 dB)
		NLOS	(3.4, 9.7 dB)
	73 GHz	LOS	(2.0, 5.2 dB)
		NLOS	(3.3, 7.6 dB)

60 to 200 m in NLOS (based on our field measurements, and may be modified):

$$d \sim U(d_{\min}, d_{\max}) \quad (8)$$

where

$$\begin{cases} d_{\min} = 30 \text{ m}, d_{\max} = 60 \text{ m}, & \text{LOS} \\ d_{\min} = 60 \text{ m}, d_{\max} = 200 \text{ m}, & \text{NLOS}. \end{cases}$$

To validate our simulation, we used the distance ranges in Step 1, but for standards work other distances are likely to be valid. Users located near BSs (i.e., small TX-RX separation) will be power controlled in the near field [27], [62].

*Step 2: Generate the total received omnidirectional power  $P_r$  (dBm) at the RX location according to the environment type:*

$$P_r(d)[\text{dBm}] = P_t[\text{dBm}] - PL(d)[\text{dB}] \quad (9)$$

$$PL[\text{dB}](d) = PL_{\text{FS}}(d_0) + 10\bar{n} \log_{10}\left(\frac{d}{d_0}\right) + \chi_\sigma \quad (10)$$

$$PL_{\text{FS}}(d_0) = 20 \times \log_{10}\left(\frac{4\pi d_0}{\lambda}\right) \quad (11)$$

where  $P_t$  is the transmit power in dBm,  $d_0 = 1$  m,  $\lambda$  is the carrier wavelength,  $\bar{n}$  is the PLE for omnidirectional TX and RX antennas, given in Table III for 28 or 73 GHz in both LOS and NLOS environments, and  $\chi_\sigma$  is the log-normal random variable with 0-dB mean and standard deviation  $\sigma$  [12]. The  $d_0 = 1$  m CI free space reference path loss model is a simple physically-based one-parameter (PLE) model [12], [33], which is more stable across frequencies and environments than the traditional FI least-squares regression equation line [12], [27], [33], [62]. Further, the CI and FI models perform similarly over identical data sets, with differences in standard deviations that are within a fraction of a dB, yet the CI model is simpler and based on fundamental propagation physics [12], [27], [33]. Also, the CI model allows the pooling of LOS power statistics at multiple mmWave frequencies without any change in model coefficients, since the PLE  $n$  is set equal to 2 for LOS propagation (this is not the case for the FI model).

*Step 3: Generate the number of TCs  $N$  and the numbers of AOD and AOA SLs ( $L_{\text{AOD}}, L_{\text{AOA}}$ ) at the RX location:*

$$N \sim DU[1, 6] \quad (12)$$

$$L_{\text{AOD}} \sim \min\left\{L_{\max}, \max\{1, \text{Poisson}(\mu_{\text{AOD}})\}\right\} \quad (13)$$

$$L_{\text{AOA}} \sim \min\left\{L_{\max}, \max\{1, \text{Poisson}(\mu_{\text{AOA}})\}\right\} \quad (14)$$

TABLE IV

KEY FREQUENCY-DEPENDENT PARAMETERS THAT REPRODUCE THE MEASURED STATISTICS OF OMNIDIRECTIONAL CHANNELS USING THE SSCM PRESENTED HEREIN FOR THE FOLLOWING FREQUENCY SCENARIOS: COMBINED 28–73-GHz LOS, 28-GHz NLOS, 73-GHz NLOS, AND COMBINED 28–73-GHz NLOS

Step #	Input Parameters	Frequency Scenario			
		28 - 73 GHz LOS	28 GHz NLOS	73 GHz NLOS	28 - 73 GHz NLOS
Step 3	$\mu_{AOD}, \mu_{AOA}$	1.9, 1.8	1.6, 1.6	1.5, 2.5	1.5, 2.1
Step 5	$X_{max}$	0.2	0.5	0.5	0.5
Step 6	$\mu_\tau [ns]$	123	83	83	83
Step 7	$\Gamma [ns], \sigma_Z [dB]$	25.9, 1	49.4, 3	56.0, 3	51.0, 3
Step 8	$\gamma [ns], \sigma_U [dB]$	16.9, 6	16.9, 6	15.3, 6	15.5, 6
Step 11b	$\mu_{AOD} [^\circ], \sigma_{AOD} [^\circ]$	-12.6, 5.9	-4.9, 4.5	-4.9, 4.5	-4.9, 4.5
	$\mu_{AOA} [^\circ], \sigma_{AOA} [^\circ]$	10.8, 5.3	3.6, 4.8	3.6, 4.8	3.6, 4.8
Step 12	$\sigma_{\theta, AOD} [^\circ], \sigma_{\phi, AOD} [^\circ]$	8.5, 2.5	9.0, 2.5	7.0, 3.5	11.0, 3.0
	$\sigma_{\theta, AOA} [^\circ], \sigma_{\phi, AOA} [^\circ]$	10.5, 11.5	10.1, 10.5	6.0, 3.5	7.5, 6.0

where  $L_{max} = 5$  is the maximum allowable number of SLs,  $\mu_{AOD}$  and  $\mu_{AOA}$  are the empirical mean number of AOD and AOA SLs, respectively (see Table IV). At 28 GHz in NLOS, the maximum number of TCs observed was 5, while it was 6 at 73 GHz, using a -10-dB threshold based on work in [38]. We therefore choose 6 to simplify the model across frequency bands. Note that in [38],  $(L_{AOD}, L_{AOA})$  were conditioned upon  $N$ , but since SPs from the same TC can arrive and depart from arbitrary directions, the number of SLs is generalized here to be independent of the number of TCs [16].

*Step 4: Generate the number of cluster SP  $M_n$  in each TC:*

$$M_n \sim DU[1, 30], \quad n = 1, 2, \dots, N. \quad (15)$$

At 28 GHz in NLOS, the maximum and second to maximum number of cluster SPs were found to be 53 and 30, respectively, over all locations, while at 73 GHz the maximum was 30 in NLOS; therefore, 30 is chosen as the upper bound of the uniform distribution for all frequencies. SP components were identified using a peak detection algorithm.

*Step 5: Generate the intracluster SP excess delays  $\rho_{m,n}$  in units of nanoseconds:*

$$\rho_{m,n}(B_{bb}) = \left\{ \frac{1}{B_{bb}} \times (m-1) \right\}^{1+X_n} \quad (16)$$

$$m = 1, 2, \dots, M_n, \quad n = 1, 2, \dots, N \quad (17)$$

where  $B_{bb} = 400$  MHz is the baseband bandwidth of the transmitted PN sequence (but can be modified for different baseband bandwidths less than 400 MHz), and  $X_n$  applies to all  $M_n$  intra-cluster SPs and is generated for the  $n$ th TC, using a uniform random variable between 0 and  $X_{max}$ . Note that  $1/B_{bb}$  must have units of nanoseconds when generating  $\rho_{m,n}$ . This step ensures a bandwidth-independent channel model, while reflecting observations that intra-cluster SP delay intervals tend to increase with delay (through the random variable  $X_n$ ). The upper bound  $X_{max}$  is easily adjustable to field measurements (see Table IV).

*Step 6: Generate the cluster excess delays  $\tau_n$ :*

$$\tau_n'' \sim \text{Exp}(\mu_\tau) \quad (18)$$

$$\Delta\tau_n = \text{sort}(\tau_n'') - \min(\tau_n'') \quad (19)$$

$$\tau_n = \begin{cases} 0, & n = 1 \\ \tau_{n-1} + \rho_{M_{n-1}, n-1} + \Delta\tau_n + 25, & n = 2, \dots, N \end{cases} \quad (20)$$

where  $\text{sort}(\cdot)$  orders the delay elements  $\tau_n''$  from smallest to largest, and where  $\mu_\tau$  is given in Table IV. This step assures no temporal cluster overlap with a 25-ns minimum inter-cluster void interval, which was found to match the measured data, and makes sense from a physical standpoint, since multipath components tend to arrive in clusters at different time delays [65] over many angular directions, most likely due to the free space air gaps between reflectors (buildings, lampposts, streets, etc). The narrowest streets have a typical spatial width of 8 m (25 ns in propagation delay) in New York City, thus physically describing the regularly observed minimum void interval for arriving energy.

*Step 7: Generate the TC powers  $P_n$  (mW):*

$$P'_n = \bar{P}_0 e^{-\frac{\tau_n}{\Gamma}} 10^{\frac{Z_n}{10}} \quad (21)$$

$$P_n = \frac{P'_n}{\sum_{k=1}^{k=N} P'_k} \times P_r [\text{mW}] \quad (22)$$

$$Z_n \sim N(0, \sigma_Z), \quad n = 1, 2, \dots, N \quad (23)$$

where  $\bar{P}_0$  is the average power in the first arriving TC,  $\Gamma$  is the cluster decay time constant, and  $Z_n$  is a lognormal random variable with 0-dB mean and standard deviation  $\sigma_Z$  (see Table IV). Equation (22) ensures that the sum of cluster powers adds up to the total omnidirectional received power  $P_r$ . Note that  $\bar{P}_0$  cancels out in (22) using (21), but can be used as a secondary statistic to validate the channel model [38]. The 3GPP, WINNER, COST, and METIS models also estimate mean cluster powers using an exponential function over time delay, as in (21) [37], [41], [42], [47].

*Step 8: Generate the cluster SP powers  $\Pi_{m,n}$  (mW):*

$$\Pi'_{m,n} = \bar{\Pi}_0 e^{-\frac{\rho_{m,n}}{\gamma}} 10^{\frac{U_{m,n}}{10}} \quad (24)$$

$$\Pi_{m,n} = \frac{\Pi'_{m,n}}{\sum_{k=1}^{M_n} \Pi'_{k,n}} \times P_n [\text{mW}] \quad (25)$$

$$U_{m,n} \sim N(0, \sigma_U) \quad (26)$$

where  $\bar{\Pi}_0$  is the average power in the first received intra-cluster SP,  $\gamma$  is the SP decay time constant, and  $U_{m,n}$  is a lognormal random variable with 0-dB mean and standard deviation  $\sigma_U$  (see Table IV);  $m = 1, 2, \dots, M_n$  and  $n = 1, 2, \dots, N$ . Equation (25) ensures that the sum of SP powers adds up to the cluster power. For model validation, the SP path losses were thresholded at 180 dB (maximum measurable path loss [12]). Note that the measurements have much greater temporal and spatial resolution than previous models. Intra-cluster power levels were observed to fall off exponentially over intra-cluster time delay (see [38, Fig. 4]).

*Step 9: Generate the SP phases  $\varphi_{m,n}$  (rad):*

$$\varphi_{m,n} \sim U(0, 2\pi) \quad (27)$$

where  $m = 1, \dots, M_n$  and  $n = 1, 2, \dots, N$ . Different from [38] where phases are estimated from frequency and delays, here the SP phases are assumed i.i.d., and uniform between 0 and  $2\pi$  [65] since each SP may experience a different scattering environment, thus arriving at arbitrary AOA SL.

*Step 10: Recover absolute time delays  $t_{m,n}$  of cluster SPs using the TX-RX separation distance  $d$  (Step 1):*

$$t_{m,n} = t_0 + \tau_n + \rho_{m,n}, \quad t_0 = \frac{d}{c} \quad (28)$$

where  $m = 1, 2, \dots, M_n$ ,  $n = 1, 2, \dots, N$ , and  $c = 3 \times 10^8$  m/s is the speed of light in free space.

*Step 11a: Generate the mean AOA and AOD azimuth angles  $\theta_i$  ( $^\circ$ ) of the 3-D SLs to avoid overlap of lobe angles:*

$$\theta_i \sim U(\theta_{\min}, \theta_{\max}), \quad i = 1, 2, \dots, L \quad (29)$$

$$\theta_{\min} = \frac{360(i-1)}{L}, \quad \theta_{\max} = \frac{360i}{L} \quad (30)$$

*Step 11b: Generate the mean AOA and AOD elevation angles  $\phi_i$  ( $^\circ$ ) of the 3-D SLs:*

$$\phi_i \sim N(\mu, \sigma), \quad i = 1, 2, \dots, L. \quad (31)$$

Values of  $\phi_i$  are defined with respect to horizon, namely, a positive and a negative value indicate a direction above and below horizon, respectively. While the 28-GHz measurements used a fixed  $10^\circ$  downtilt at the TX, and considered elevation planes of  $0^\circ$ , and  $\pm 20^\circ$  at the RX, mmWave transceivers will most likely beamform in the strongest directions, as emulated in the 73-GHz measurements [27]. Consequently, the provided elevation angle distributions for all frequency scenarios are extracted from the 73-GHz measurements (see Table IV).

*Step 12: Generate the AOD angles ( $\theta_{m,n,\text{AOD}}$ ,  $\phi_{m,n,\text{AOD}}$ ) and AOA angles ( $\theta_{m,n,\text{AOA}}$ ,  $\phi_{m,n,\text{AOA}}$ ) of each SP component*

using the SL angles found in Step 11:

$$\theta_{m,n,\text{AOD}} = \theta_i + (\Delta\theta_i)_{m,n,\text{AOD}} \quad (32)$$

$$\phi_{m,n,\text{AOD}} = \phi_i + (\Delta\phi_i)_{m,n,\text{AOD}} \quad (33)$$

$$\theta_{m,n,\text{AOA}} = \theta_j + (\Delta\theta_j)_{m,n,\text{AOA}} \quad (34)$$

$$\phi_{m,n,\text{AOA}} = \phi_j + (\Delta\phi_j)_{m,n,\text{AOA}} \quad (35)$$

where

$$i \sim \text{DU}[1, L_{\text{AOD}}], \quad j \sim \text{DU}[1, L_{\text{AOA}}] \quad (36)$$

$$(\Delta\theta_i)_{m,n,\text{AOD}} \sim N(0, \sigma_{\theta,\text{AOD}}) \quad (37)$$

$$(\Delta\phi_i)_{m,n,\text{AOD}} \sim N(0, \sigma_{\phi,\text{AOD}}) \quad (38)$$

$$(\Delta\theta_j)_{m,n,\text{AOA}} \sim N(0, \sigma_{\theta,\text{AOA}}) \quad (39)$$

$$(\Delta\phi_j)_{m,n,\text{AOA}} \sim \text{Laplace}(\sigma_{\phi,\text{AOA}}). \quad (40)$$

This step assigns to each multipath component a single spatial AOD and AOA lobe in a uniform random fashion, in addition to a random angular offset within the SL with distributions specified in (37)–(40). Note that the Laplace distribution in (40) provided a better fit to all data across frequencies and environments than a normal distribution. The 3GPP model uses a uniform distribution from  $-40^\circ$  to  $+40^\circ$  to generate path azimuth AODs, and for path azimuth AOAs uses a zero-mean normal distribution whose variance is a function of path powers for the UMi scenario [41]. The WINNER models use a wrapped Gaussian distribution to generate path AODs and AOAs [42].

## B. SSCM Implementation

*1) CIRs at a Particular T-R Separation Distance:* To facilitate the implementation of this SSCM, Tables III and IV provide the necessary parameters required in Steps 2, 3, 5–8, 11b, and 12 for generating CIRs at a particular T-R separation distance as a function of the frequency-scenarios considered in this work. The SSCM also incorporates polarization effects, through the use of complex-amplitude antenna patterns [see (5)], which specify the amplitude *and* phase induced by an antenna beam for  $(\theta, \phi)$  angles. Cross-polarization losses can be accounted for in the omnidirectional path loss (see Step 2 in Section V-A) using available mmWave cross-polarization path loss models, as described in [12] and [27] providing cross-polarization discrimination factors for indoor and outdoor mmWave channels. Finally, XPR statistics of individual multipath components have been measured and modeled by a Gaussian lognormal distribution to account for mmWave channel depolarization [17].

*2) Local Area CIR:* Small-scale spatial fading of individual 2.5-ns resolvable multipath components were measured and shown to follow a Rician distribution with  $K$ -factors in the range 9–15 and 3–7 dB in vertical-to-vertical (V-V) and vertical-to-horizontal (V-H) LOS channels, respectively, and with  $K$ -factors in the range 5–8 and 3–7 dB in V-V and V-H NLOS channels, respectively [70]. The autocorrelation of individual multipath amplitudes was accurately modeled with an exponential function over antenna separation distance [70]. Knowledge of mmWave small-scale fading distributions and autocorrelation of individual multipath components

has allowed for realistic 5G MIMO system-level simulations as demonstrated in [69]. The MIMO channel matrix  $H_l$  for the  $l$ th multipath component, between a transmitter with  $N_t$  antenna elements and a receiver with  $N_r$  antenna elements, is computed as in [69]

$$H_l = R_r^{1/2} H_w R_t^{1/2} \quad (41)$$

where  $H_w$  is an  $N_t \times N_r$  matrix with entries generated from an i.i.d. Rician distribution, and  $R_t$  and  $R_r$  are the transmit and receive spatial correlation matrices for user-defined antenna arrays (e.g., uniform linear array, uniform rectangular array) [69]. The statistical channel models presented in Section V-A have been implemented in a MATLAB-based simulator, which generates CIRs at a particular T-R separation distance and local area omnidirectional and directional CIRs, with complementary MATLAB source files freely downloadable in [18].

3) *Track or Grid CIR*: The time-varying channel coefficients along a moving receiver can be obtained by accounting for the Doppler phase shifts of individual multipaths, based on the multipath AOA and receiver velocity vector. The large-scale spatially varying birth and death of TCs and SLs are analogous to the 3GPP birth and death processes defined for delay-angular clusters [41], [42], and can be used to enable realistic MU-MIMO simulations over a user-defined trajectory along a track or grid of points. Knowledge of the autocorrelation for the number of TCs and SLs as a function of MS distance for closely spaced location points with known CIRs offers the possibility of implementing statistical CIRs over a track or grid of points. The spatial autocorrelation between two MSs with separation distance  $d_{MS}$  for the number of SLs and the number of TCs can be computed as in [69],

$$\rho(d_{MS}) = \frac{E[L(r + d_{MS})L(r)] - E[L(r + d_{MS})]E[L(r)]}{\sigma[L(r + d_{MS})]\sigma[L(r)]} \quad (42)$$

where

$$\sigma[L(r)] = \sqrt{E[L(r) - E[L(r)]]^2} \quad (43)$$

where  $L(r)$  is the number of SLs or the number of TCs at T-R separation  $r$ ,  $E[\cdot]$  is the expectation operator over all possible values of  $r$ , and  $\sigma[L(r)]$  is the standard deviation of the number of TC or SL at distance  $r$ .

### C. Sample Output Functions

Figs. 15 and 16 show example output functions of a 28-GHz NLOS omnidirectional PDP, and corresponding AOA 3-D power spectrum, obtained from a MATLAB-based statistical simulator that implemented the channel models given in (8)–(40). The generated PDP in Fig. 15 is composed of four multipath taps, grouped into two TCs with exponentially decaying amplitudes with cluster decay constant  $\Gamma = 49.4$  ns and intra-cluster SP decay constant  $\gamma = 16.9$  ns (see Steps 6 and 7 in Section V-A). Here, a transmit power of 30 dBm is used with a noise threshold set to  $-100$  dBm over an 800-MHz RF bandwidth, and the simulated PDP has a total omnidirectional path loss of 120 dB with a TX-RX separation

### Sample Omni. PDP Output Function

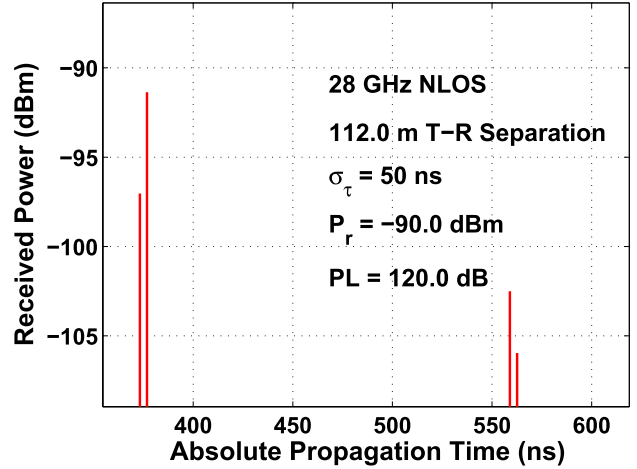


Fig. 15. Example of simulated 28-GHz NLOS PDP obtained from the MATLAB-based statistical simulator.

### 3-D AOA Power Spectrum - 28 GHz NLOS

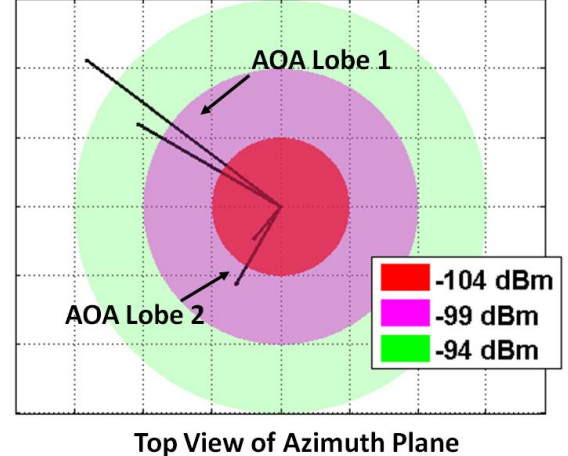


Fig. 16. Example of simulated 28-GHz NLOS 3-D AOD power spectrum obtained from the MATLAB-based statistical simulator. This spectrum is associated with the PDP shown in Fig. 15.

distance of 112 m, an RMS DS of 50 ns, and 0-dBi TX and RX antenna gains. The AOA spectrum (Fig. 16) shows the four multipath taps grouped into two AOA SLs according to (34), (35), (39), and (40). Note that the multipaths in Fig. 16 may be convolved with an arbitrary antenna pattern to study the effects of antenna beamwidths on the CIR.

The 28- and 73-GHz NLOS cluster and SP power parameters  $\Gamma$  and  $\gamma$  shown in Table III (rows 4 and 5) are similar, with  $\Gamma = 49.4$  ns (28 GHz) and  $\Gamma = 56.0$  ns (73 GHz) and with  $\gamma = 16.9$  ns (28 GHz) and  $\gamma = 15.3$  ns (73 GHz), obtained with a 25-ns minimum inter-cluster void interval. The  $(\Gamma, \gamma)$  parameters were extracted for various values of minimum inter-cluster void interval, namely, 15 and 20 ns, and showed similar parameter values across frequency bands indicating similar channel dynamics at 28 and 73 GHz. However, note that the cluster and SP decay constants  $(\Gamma, \gamma)$  obtained with a 25-ns minimum intercluster void interval recreated the measured statistics most accurately.

The channel models provided herein are valid for a 2.5-ns multipath time resolution (800 MHz) and antenna beamwidths of 7°–10° [16]. However, it is also possible to synthesize omnidirectional and directional CIRs for bandwidths less than 800 MHz and for angular resolutions greater than 7°. In the time domain, it is sufficient to coherently sum (e.g., convolve) the multipath components that fall within a time bin width equal to the inverse of the desired bandwidth. For instance, for a desired RF channel bandwidth of 400 MHz (200-MHz baseband bandwidth), a user may coherently sum the multipath amplitudes in (4) (valid for a 2.5-ns time resolution) that fall within a bin width of 5 ns. The angular resolution of the resulting IR can be adjusted by convolving the SSCM output with a 3-D complex antenna pattern with HPBW greater than 7°, in (5) and (45) [16]. The first- and second-order statistics, as well as the cumulative distribution function (CDF) tail behavior of simulated directional RMS DSs were properly recreated using past published measurements that used a wide range of beamwidths and bandwidths [11], [13], [59], as shown in Fig. 19.

## VI. SIMULATION RESULTS

The statistical channel model presented in (8)–(40) was used to implement a MATLAB-based statistical simulator to verify and validate the accuracy of the simulated temporal and spatial statistics when compared against the measured statistics. A large simulation was carried out for each of the four frequency scenarios presented in this work, in which 10 000 omnidirectional PDPs, and 3-D AOD and AOA power spectra were generated as sample functions of (4). We used simple number generators to obtain the number of TCs, the numbers of AOD and AOA SLs, cluster and SP delays, and cluster and SP powers, as described in Section V-A. We set the TX power to 30 dBm and assume a noise floor of –100 dBm over an 800-MHz RF bandwidth, with the TX and RX antenna gains set to 24.5 and 27 dBi to emulate the 28- and 73-GHz measurements [11], [57] when performing directional simulations.

### A. Simulated Omnidirectional Path Loss

Fig. 17 shows the 28-GHz simulated omnidirectional LOS and NLOS path losses obtained using the statistical channel model presented in (8)–(28). The LOS and NLOS conditions used in the SSCM were determined based on a probabilistic function describing the LOS probability  $P_{\text{LOS}}(d)$  between a transmitter and a receiver in a dense urban microcellular environment, obtained using 3-D ray-tracing techniques as proposed in [35]

$$P_{\text{LOS}}(d) = \left[ \min \left( \frac{d_{\text{BP}}}{d}, 1 \right) \left( 1 - e^{-\frac{d}{\alpha}} \right) + e^{-\frac{d}{\alpha}} \right]^2 \quad (44)$$

where  $d_{\text{BP}} = 27$  m and  $\alpha = 71$  m. Steps 1–10 of Section V-A were implemented to recover LOS and NLOS wideband PDPs, and the corresponding path losses were computed by subtracting the total received power (dBm) from the TX power (dBm) for each of the simulated profiles. The simulated PLE and large-scale shadow factor were 2.0 and 3.6 dB in LOS, and 3.4 and 9.7 dB in NLOS, respectively, which are in agreement

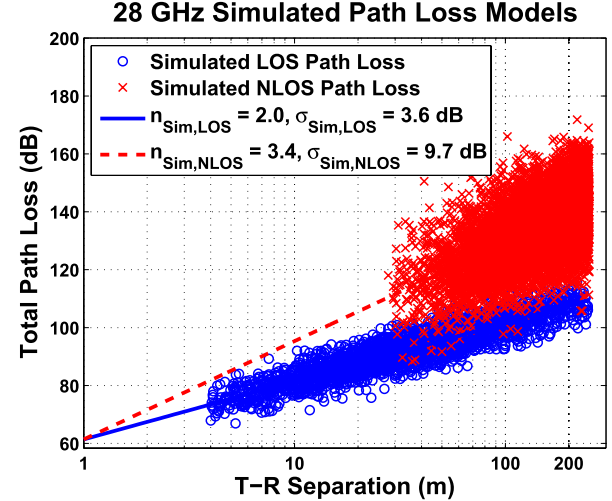


Fig. 17. Example of 28-GHz simulated omnidirectional LOS and NLOS path loss results obtained from 10 000 sample functions using the SSCM described herein. There is excellent agreement between simulated and measured PLEs and shadow factors.

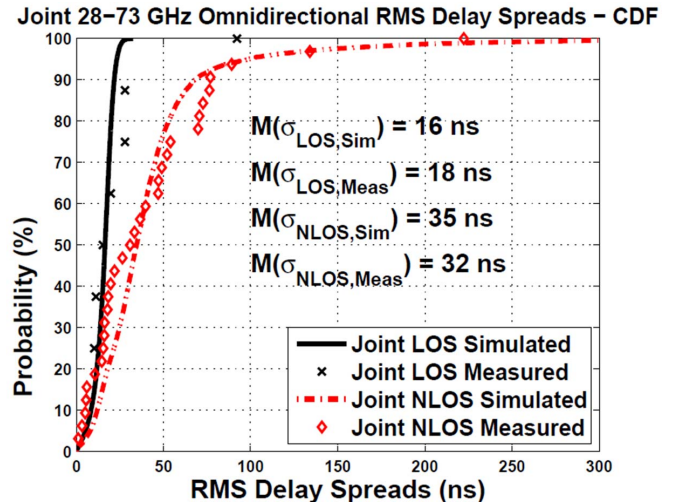


Fig. 18. Combined 28–73-GHz LOS and NLOS omnidirectional RMS DSs synthesized from absolute timing PDPs, superimposed with the simulation results of RMS DSs obtained from 10 000 sample functions using the SSCM described herein [16].

with the measured parameters shown in Table III and in [27]. The simulated statistics match the measured statistics very well, over a large ensemble of generated channels, and can be used to realistically reproduce the measurements in the context of a system-level simulation.

### B. Simulated RMS Delay Spreads

The RMS DS describes channel temporal dispersion, and is a vital statistic that an SSCM should reproduce faithfully. Fig. 18 shows the simulated omnidirectional RMS DSs, compared with the RMS DSs obtained from the absolute timing PDPs, at both 28 and 73 GHz in LOS and NLOS scenarios. We obtained 18 and 16 ns for the empirical and simulated medians, respectively, for the combined 28–73-GHz LOS scenario, and 32 and 35 ns for the empirical and simulated medians, respectively, for the combined 28–73-GHz NLOS scenario. The lack of measured data considerably skewed the empirical distributions, so the median was chosen

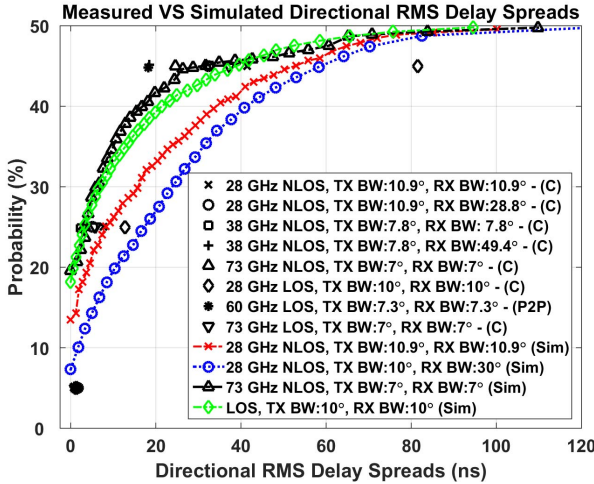


Fig. 19. Simulated directional RMS DS CDFs (lines) for various frequencies and for antenna beamwidths, obtained from directional PDPs generated using (5). Values reported from the literature are shown as points [11], [13], [59]. C stands for cellular, and P2P stands for peer-to-peer.

to represent the distribution trend. The empirical and simulated medians in NLOS were 31 and 32 ns at 28 GHz (see [38, Fig. 5]), respectively, and 47 and 39 ns at 73 GHz, respectively, showing good agreement with empirical values. The strong agreement between simulated and empirical distributions validates the temporal component of the SSCM.

The SSCM model can also recreate *directional PDPs* at arbitrary TX-RX pointing angle combination for user-defined azimuth and elevation antenna HPBWs. It is possible to reconstruct the temporal and spatial statistics of arbitrary antenna beamwidths by weighting the multipath component power levels with a desired antenna pattern, such that the multipath components closest to a desired direction are amplified, while those farthest away are effectively set to 0, as shown in (5).

When simulating directional PDPs, the multipath components were weighted by  $G_{\text{TX}}(\theta, \phi)$  and  $G_{\text{RX}}(\theta, \phi)$ , the TX and RX antenna patterns, respectively, commonly parameterized as follows [72]:

$$G(\theta, \phi) = \max \left( G_0 e^{\alpha \theta^2 + \beta \phi^2}, \frac{G_0}{100} \right) \quad (45)$$

$$\alpha = \frac{4 \ln(2)}{\theta_{3\text{dB}}^2}, \quad \beta = \frac{4 \ln(2)}{\phi_{3\text{dB}}^2}, \quad G_0 = \frac{41253 \eta}{\theta_{3\text{dB}} \phi_{3\text{dB}}} \quad (46)$$

where  $(\theta, \phi)$  are the azimuth and elevation angle offsets from the boresight direction in degrees,  $G_0$  is the maximum directive gain (boresight gain) in linear units,  $(\theta_{3\text{dB}}, \phi_{3\text{dB}})$  are the azimuth and elevation HPBWs in degrees,  $\alpha, \beta$  are parameters that depend on the HPBW values, and  $\eta = 0.7$  is a typical average antenna efficiency.

Fig. 19 shows simulated directional RMS DSs obtained from the 28- and 73-GHz channel models presented here, in comparison with reported values in the literature for the 10%, 50%, and 90% CDF points of measured directional RMS DSs at 28, 38, 60, and 73 GHz [13], [31], [73], [74], for antenna beamwidths of 7.3°, 10.9°, 28.8°, and 49.4°. To test (5), we generated omnidirectional sample functions using the presented SSCM, convolved (multiplied) the omnidirectional CIRs with the simulated antenna patterns [see (45)],

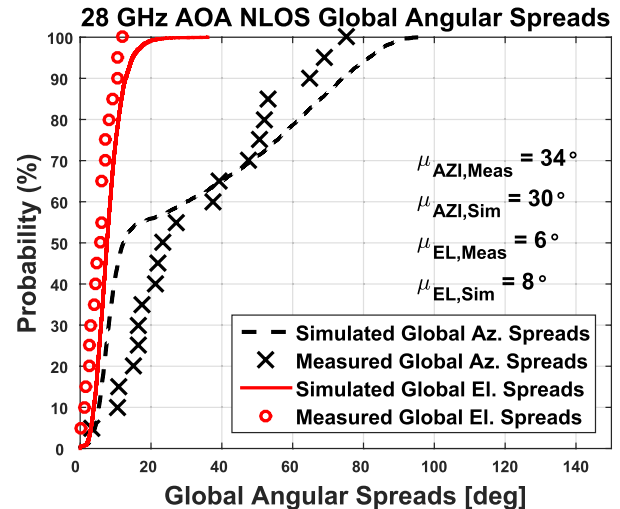


Fig. 20. 28-GHz NLOS global AS and elevation spread, obtained from the NYC measurements [12] and the 3-D SSCM.

and computed directional RMS DSs from directional PDPs obtained using (5) for 20 T-R separation distances using antenna HPBWs of 10°, 7°, and 30° in azimuth/elevation at 28 and 73 GHz to emulate the NYC measurements. Note the empirical CDFs consist of all available data, while the simulated directional RMS DSs were obtained from channel models extracted exclusively from up to four strongest AOD and AOA PDP data. Fig. 19 shows the simulated and measured RMS DS distributions match relatively well across antenna beamwidths and many mmWave bands.

### C. Simulated RMS Angular Spreads

The omnidirectional azimuth and elevation spreads describe the degree of angular dispersion at a BS or MS over the entire  $4\pi$  steradian sphere [41], [42], also termed *global* angular spreads in [17] and [47]. The AOD and AOA global angular spreads were computed from all available 28 and 73 GHz NLOS measured data, using the total (integrated over delay) received power at unique azimuth/elevation pointing angles, but not requiring absolute multipath time delays, and the equations in [41, Annex A]. These were compared with the simulated angular spreads using the 3-D SSCM, where the SSCM was developed from the statistics of up to four strong measured angles. The simulated and measured mean global angular spreads match relatively well at 28 and 73 GHz, as can be seen from Figs. 20 and 21. The slight differences (slight under-estimation or over-estimation of global ASs using Step 12 in Section V-A) may be due to the model focusing only on the multipath components contained in the strongest several SLs measured at every location, which will in actuality be the strongest components in a practical wireless system.

The directional AOD and AOA RMS *lobe* AS and elevation spread were also computed based on a  $-10$  dB lobe threshold [38] from the 28 and 73 GHz data, and compared with simulated values using the 3-D SSCM. Fig. 22 shows typical measured against simulated AOA RMS lobe angular spreads for the 73-GHz NLOS scenario, showing an excellent match over the empirical and simulated means of  $4^\circ$  and  $2^\circ$  in

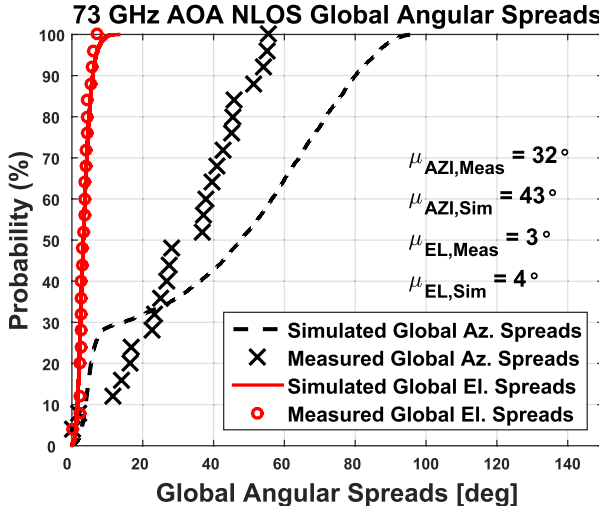


Fig. 21. 73-GHz NLOS global AS and elevation spread, obtained from the NYC measurements [12] and the 3-D SSCM.

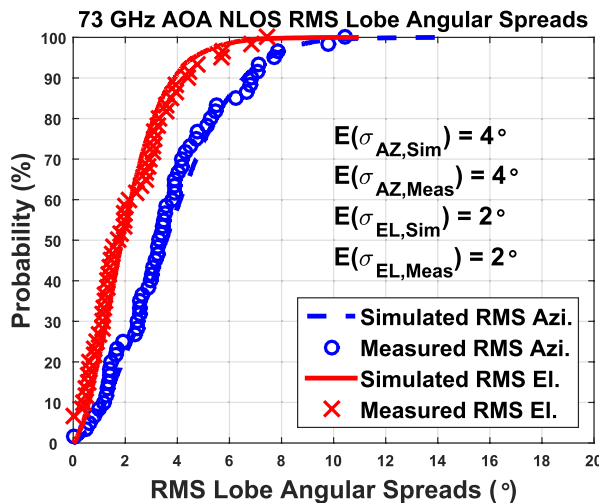


Fig. 22. 73-GHz NLOS AOA RMS AS and elevation spread, measured and simulated, showing good agreement [38]. Only non-zero simulated RMS lobe angular spreads are plotted, to provide a fair comparison with the measurements. Approximately 4% of the simulated data yielded zero-valued RMS lobe angular spreads (e.g., only a single angular segment in a lobe).

azimuth and elevation, respectively, over all measured SLs. Similar agreement was found for the 28-GHz NLOS and LOS data sets, across AOD and AOA SLs, indicating that the model accurately recreates the empirical spatial statistics. Fig. 21 shows only non-zero simulated RMS lobe angular spreads, to remain consistent with field observations that showed that all the measured SLs are composed of at least two multipath components, corresponding to non-zero rms lobe angular spreads. However, approximately 4% of all simulated data was composed of zero-valued RMS lobe angular spreads, physically denoting that 4% of all SLs are composed of just one multipath component (e.g., zero angle spread in a lobe).

## VII. DISCUSSION

Twelve thousand measured PDPs have been used to create a statistical channel model that reproduces realistic wideband

power IRs and joint AOD-AOA power spectra in 3-D based on the 28 and 73 GHz New York City measurements.  $L_{\text{AOD}}$ , the average number of AOD SLs at the transmitter, is Poisson distributed and frequency independent with a mean of about 2 and 1.5 in LOS and NLOS environments, respectively, indicating that strong multipath signals can reach the receiver from more departing angles in LOS compared to NLOS. However,  $L_{\text{AOA}}$ , the average number of AOA SLs at the receiver, is frequency dependent, with a mean of 1.6 and 2.5 at 28 and 73 GHz in NLOS, respectively, implying more pronounced diffuse scattering with increasing carrier frequency. SLs conveniently represent the mmWave radio channel because they implicitly account for directionality, a key differentiator of future wireless cellular and mobile systems operating in the mmWave spectrum compared with today's UHF and microwave systems.

TC and SP powers were shown to decay exponentially with little dependence on the carrier frequency, with typical  $\Gamma$  and  $\gamma$  of 25 and 17 ns in LOS, and 51 and 16 ns, in NLOS, respectively, when combining the 28 and 73 GHz data sets, using a 25-ns minimum intercluster void interval. In some cases, TCs can carry up to 80% of the total received power at excess delays larger than 100 ns, thus inducing large RMS DSSs.

## VIII. CONCLUSION

This paper presented a 3-D statistical channel model for mmWave LOS and NLOS communications for link, local area, and track CIRs, with arbitrary carrier frequency, signal bandwidth, and antenna beamwidth, invaluable in the design of next-generation 5G mmWave cellular networks. The simplicity of the presented statistical IR model stems from the independent modeling of time and space, allowing for simple statistical distributions to promote ease of use in simulated software and hardware implementations, while reproducing physically based CIRs and 3-D power angular spectra based on real-world measurements. Arbitrary antenna beamwidths and frequency are supported, and we showed good agreement between the model and published RMS DSSs. The TCSL model parameters, provided in Table II, may be included as simple extensions to existing 3GPP parameters to account for observed mmWave channel directionality, as given in [17]. A MATLAB-based statistical simulator, available in [18], was implemented to generate a large ensemble of PDPs and 3-D power angular spectra, showing good agreement with field measurements, thereby validating the 3-D SSCM for the design of next-generation wireless systems that will make use of sub-6 GHz and mmWave channel models for the design of filters, multielement antenna arrays, and mmWave transceivers.

## ACKNOWLEDGMENT

The authors would like to thank S. Sun, G. R. MacCartney Jr., and the NYU WIRELESS Industrial Affiliates for their support, and Prof. H. Bertoni and Prof. S. Rangan for valuable discussions.

## REFERENCES

- [1] K. Haneda *et al.*, "5G 3GPP-like channel models for outdoor urban microcellular and macrocellular environments," in *Proc. IEEE 83rd Veh. Technol. Conf. (VTC-Spring)*, May 2016.

- [2] K. Haneda *et al.*, "Indoor 5G 3GPP-like channel models for office and shopping mall environments," in *Proc. IEEE Int. Conf. Commun. (ICC) Workshops*, May 2016.
- [3] L. Lu, G. Y. Li, A. L. Swindlehurst, A. Ashikhmin, and R. Zhang, "An overview of massive MIMO: Benefits and challenges," *IEEE J. Sel. Topics Signal Process.*, vol. 8, no. 5, pp. 742–758, Oct. 2014.
- [4] E. G. Larsson, O. Edfors, F. Tufvesson, and T. L. Marzetta, "Massive MIMO for next generation wireless systems," *IEEE Commun. Mag.*, vol. 52, no. 2, pp. 186–195, Feb. 2014.
- [5] V. Garcia, Y. Zhou, and J. Shi, "Coordinated multipoint transmission in dense cellular networks with user-centric adaptive clustering," *IEEE Trans. Wireless Commun.*, vol. 13, no. 8, pp. 4297–4308, Aug. 2014.
- [6] V. Jungnickel *et al.*, "The role of small cells, coordinated multipoint, and massive MIMO in 5G," *IEEE Commun. Mag.*, vol. 52, no. 5, pp. 44–51, May 2014.
- [7] G. Nigam, P. Minero, and M. Haenggi, "Coordinated multipoint joint transmission in heterogeneous networks," *IEEE Trans. Commun.*, vol. 62, no. 11, pp. 4134–4146, Nov. 2014.
- [8] Z. Khan, H. Ahmadi, E. Hossain, M. Coupechoux, L. A. Dasilva, and J. J. Lehtomäki, "Carrier aggregation/channel bonding in next generation cellular networks: Methods and challenges," *IEEE Netw.*, vol. 28, no. 6, pp. 34–40, Nov. 2014.
- [9] F. Khan and Z. Pi, "mmWave mobile broadband (MMB): Unleashing the 3–300GHz spectrum," in *Proc. 34th IEEE Sarnoff Symp.*, May 2011, pp. 1–6.
- [10] T. S. Rappaport, R. W. Heath, Jr., R. C. Daniels, and J. N. Murdock, *Millimeter Wave Wireless Communications*. Englewood Cliffs, NJ, USA: Prentice-Hall, 2015.
- [11] T. S. Rappaport *et al.*, "Millimeter wave mobile communications for 5G cellular: It will work!" *IEEE Access*, vol. 1, pp. 335–349, May 2013.
- [12] T. S. Rappaport, G. R. Maccartney, Jr., M. K. Samimi, and S. Sun, "Wideband millimeter-wave propagation measurements and channel models for future wireless communication system design," *IEEE Trans. Commun.*, vol. 63, no. 9, pp. 3029–3056, Sep. 2015.
- [13] T. S. Rappaport, F. Gutierrez, Jr., E. Ben-Dor, J. N. Murdock, Y. Qiao, and J. I. Tamir, "Broadband millimeter-wave propagation measurements and models using adaptive-beam antennas for outdoor urban cellular communications," *IEEE Trans. Antennas Propag.*, vol. 61, no. 4, pp. 1850–1859, Apr. 2013.
- [14] A. Maltsev *et al.*, "WP5: Propagation, antennas and multi-antenna techniques—D5.1: Channel modeling and characterization," *Millim.-Wave Evol. Backhaul Access (MiWEBA)*, Jun. 2014.
- [15] M. K. Samimi *et al.*, "28 GHz angle of arrival and angle of departure analysis for outdoor cellular communications using steerable beam antennas in New York City," in *Proc. IEEE 77th Veh. Technol. Conf. (VTC Spring)*, Jun. 2013, pp. 1–6.
- [16] M. K. Samimi and T. S. Rappaport, "Statistical channel model with multi-frequency and arbitrary antenna beamwidth for millimeter-wave outdoor communications," in *Proc. IEEE Globecom Workshops*, Dec. 2015, pp. 1–7.
- [17] M. K. Samimi and T. S. Rappaport, "Local multipath model parameters for generating 5G millimeter-wave 3GPP-like channel impulse response," in *Proc. 10th Eur. Conf. Antennas Propag. (EuCAP)*, Apr. 2016, pp. 1–5.
- [18] NYU WIRELESS. *Open Source Downloadable 5G Channel Simulator Software*, accessed on Apr. 2016. [Online]. Available: <http://bit.ly/1WNPpDX>
- [19] P. Soma, Y. W. -M. Chia, and L. C. Ong, "Modeling and analysis of time varying radio propagation channel for LMDS," in *Proc. IEEE Radio Wireless Conf. (RAWCON)*, Sep. 2000, pp. 115–118.
- [20] A. F. Elrefaei and M. Shakouri, "Propagation measurements at 28 GHz for coverage evaluation of local multipoint distribution service," in *Proc. Wireless Commun. Conf.*, Aug. 1997, pp. 12–17.
- [21] S. Y. Seidel, "Radio propagation and planning at 28 GHz for local multipoint distribution service (LMDS)," in *Proc. IEEE Antennas Propag. Soc. Int. Symp.*, vol. 2. Jun. 1998, pp. 622–625.
- [22] S. Geng, J. Kivinen, X. Zhao, and P. Vainikainen, "Millimeter-wave propagation channel characterization for short-range wireless communications," *IEEE Trans. Veh. Technol.*, vol. 58, no. 1, pp. 3–13, Jan. 2009.
- [23] H. Xu, V. Kukshya, and T. S. Rappaport, "Spatial and temporal characteristics of 60-GHz indoor channels," *IEEE J. Sel. Areas Commun.*, vol. 20, no. 3, pp. 620–630, Apr. 2002.
- [24] P. Soma, L. C. Ong, S. Sun, and M. Y. W. Chia, "Propagation measurements and modeling of LMDS radio channel in Singapore," *IEEE Trans. Veh. Technol.*, vol. 52, no. 3, pp. 595–606, May 2003.
- [25] P. F. M. Smulders and A. G. Wagemans, "Wideband indoor radio propagation measurements at 58 GHz," *Electron. Lett.*, vol. 28, no. 13, pp. 1270–1272, Jun. 1992.
- [26] P. F. M. Smulders and A. G. Wagemans, "A statistical model for the MM-wave indoor radio channel," in *Proc. 3rd IEEE Int. Symp. Pers., Indoor Mobile Radio Commun. (PIMRC)*, Oct. 1992, pp. 303–307.
- [27] G. R. Maccartney, Jr., T. S. Rappaport, S. Sun, and S. Deng, "Indoor office wideband millimeter-wave propagation measurements and channel models at 28 and 73 GHz for ultra-dense 5G wireless networks," *IEEE Access*, vol. 3, pp. 2388–2424, 2015.
- [28] W. Roh *et al.*, "Millimeter-wave beamforming as an enabling technology for 5G cellular communications: Theoretical feasibility and prototype results," *IEEE Commun. Mag.*, vol. 52, no. 2, pp. 106–113, Feb. 2014.
- [29] K. Haneda, J. Järveläinen, A. Karttunen, M. Kyrö, and J. Putkonen, "Indoor short-range radio propagation measurements at 60 and 70 GHz," in *Proc. 8th Eur. Conf. Antennas Propag. (EuCAP)*, Apr. 2014, pp. 634–638.
- [30] R. Müller *et al.*, "Ultra-wideband channel sounder for measurements at 70 GHz," in *Proc. IEEE Veh. Technol. Conf. (VTC)*, May 2014, pp. 1–5.
- [31] G. R. Maccartney, Jr., M. K. Samimi, and T. S. Rappaport, "Exploiting directionality for millimeter-wave wireless system improvement," in *Proc. IEEE Int. Conf. Commun. (ICC)*, Jun. 2015, pp. 2416–2422.
- [32] S. Hur *et al.*, "Proposal on millimeter-wave channel modeling for 5G cellular system," *IEEE J. Sel. Topics Signal Process.*, vol. 10, no. 3, pp. 454–469, Apr. 2016.
- [33] S. Sun *et al.*, "Investigation of prediction accuracy, sensitivity, and parameter stability of large-scale propagation path loss models for 5G wireless communications," *IEEE Trans. Veh. Technol.*, vol. 65, no. 5, pp. 2843–2860, May 2016.
- [34] T. S. Thomas, H. C. Nguyen, G. R. MacCartney, Jr., and T. S. Rappaport, "3D mmWave channel model proposal," in *Proc. IEEE 80th Veh. Technol. Conf. (VTC Fall)*, Sep. 2014, pp. 1–6.
- [35] M. K. Samimi, T. S. Rappaport, and G. R. MacCartney, Jr., "Probabilistic omnidirectional path loss models for millimeter-wave outdoor communications," *IEEE Wireless Commun. Lett.*, vol. 4, no. 4, pp. 357–360, Aug. 2015.
- [36] H. C. Nguyen, G. R. MacCartney, Jr., T. Thomas, T. S. Rappaport, B. Vejlgaard, and P. Mogensen, "Evaluation of empirical ray-tracing model for an urban outdoor scenario at 73 GHz E-band," in *Proc. IEEE 80th Veh. Technol. Conf. (VTC Fall)*, Sep. 2014, pp. 1–6.
- [37] V. Nurmela *et al.*, "Deliverable D1.4: METIS channel models," *Mobile Wireless Commun. Enablers Twenty-Twenty Inf. Soc. (METIS)*, Apr. 2014.
- [38] M. K. Samimi and T. S. Rappaport, "3-D statistical channel model for millimeter-wave outdoor mobile broadband communications," in *Proc. IEEE Int. Conf. Commun. (ICC)*, Jun. 2015, pp. 2430–2436.
- [39] S. Sun, T. S. Rappaport, R. W. Heath, Jr., A. Nix, and S. Rangan, "MIMO for millimeter-wave wireless communications: Beamforming, spatial multiplexing, or both?" *IEEE Commun. Mag.*, vol. 52, no. 12, pp. 110–121, Dec. 2014.
- [40] M. K. Samimi and T. S. Rappaport, "Ultra-wideband statistical channel model for non line of sight millimeter-wave urban channels," in *Proc. IEEE Global Commun. Conf. (GLOBECOM)*, Dec. 2014, pp. 3483–3489.
- [41] *Spatial Channel Model for Multiple Input Multiple Output (MIMO) Simulations*, document 3GPP TR 25.996 V12.0.0, Sep. 2014.
- [42] P. Kyösti *et al.*, "WINNER II channel models," Eur. Commission, Tech. Rep. D1.1.2 V1.1, Sep. 2007. [Online]. Available: <http://projects.celticinitiative.org/winner-II/WINNER2-Deliverables/>
- [43] A. Algans, K. I. Pedersen, and P. E. Mogensen, "Experimental analysis of the joint statistical properties of azimuth spread, delay spread, and shadow fading," *IEEE J. Sel. Areas Commun.*, vol. 20, no. 3, pp. 523–531, Apr. 2002.
- [44] G. Calcev *et al.*, "A wideband spatial channel model for system-wide simulations," *IEEE Trans. Veh. Technol.*, vol. 56, no. 2, pp. 389–403, Mar. 2007.
- [45] B. H. Fleury, M. Tschudin, R. Heddergott, D. Dahlhaus, and K. I. Pedersen, "Channel parameter estimation in mobile radio environments using the SAGE algorithm," *IEEE J. Sel. Areas Commun.*, vol. 17, no. 3, pp. 434–450, Mar. 1999.
- [46] N. Czink, P. Cera, J. Salo, E. Bonek, J.-P. Nuutinen, and J. Ylitalo, "A framework for automatic clustering of parametric MIMO channel data including path powers," in *Proc. IEEE 64th Veh. Technol. Conf. (VTC Fall)*, Sep. 2006, pp. 1–5.
- [47] L. Liu *et al.*, "The COST 2100 MIMO channel model," *IEEE Wireless Commun.*, vol. 19, no. 6, pp. 92–99, Dec. 2012.

- [48] R. Verdone and A. Zanella, (Eds.), *Pervasive Mobile and Ambient Wireless Communications: COST Action 2100*. London, U.K.: Springer-Verlag London Ltd., 2012.
- [49] T. S. Rappaport, S. Y. Seidel, and K. Takamizawa, "Statistical channel impulse response models for factory and open plan building radio communicate system design," *IEEE Trans. Commun.*, vol. 39, no. 5, pp. 794–807, May 1991.
- [50] T. S. Rappaport, W. Huang, and M. J. Feuerstein, "Performance of decision feedback equalizers in simulated urban and indoor radio channels," *IEICE Trans. Commun.*, vol. E76-B, no. 2, pp. 78–89, Feb. 1993.
- [51] T. S. Rappaport, S. Y. Seidel, and R. Singh, "900-MHz multipath propagation measurements for US digital cellular radiotelephone," *IEEE Trans. Veh. Technol.*, vol. 39, no. 2, pp. 132–139, May 1990.
- [52] S. Y. Seidel, T. S. Rappaport, S. Jain, M. L. Lord, and R. Singh, "Path loss, scattering and multipath delay statistics in four European cities for digital cellular and microcellular radiotelephone," *IEEE Trans. Veh. Technol.*, vol. 40, no. 4, pp. 721–730, Nov. 1991.
- [53] T. S. Rappaport, *Wireless Communications: Principles and Practice* (Prentice-Hall Commun. Eng. Emerg. Technol. Series), 2nd ed. Upper Saddle River, NJ, USA: Prentice-Hall, 2002.
- [54] J. E. Nuckols, "Implementation of geometrically based single-bounce models for simulation of angle-of-arrival of multipath delay components in the wireless channel simulation tools, SMRCIM and SIRCIM," M.S. thesis, Dept. Elect. Eng., Virginia Polytech. Inst. and State Univ., Blacksburg, VA, USA, 1999.
- [55] K. Yu, M. Bengtsson, B. Ottersten, D. McNamara, P. Karlsson, and M. Beach, "A wideband statistical model for NLOS indoor MIMO channels," in *Proc. IEEE 55th Veh. Technol. Conf. (VTC-Spring)*, vol. 1, May 2002, pp. 370–374.
- [56] B. Han and Y. R. Zheng, "Higher rank principal Kronecker model for triply selective fading channels with experimental validation," *IEEE Trans. Veh. Technol.*, vol. 64, no. 5, pp. 1654–1663, May 2015.
- [57] G. R. MacCartney, Jr., and T. S. Rappaport, "73 GHz millimeter wave propagation measurements for outdoor urban mobile and back-haul communications in New York City," in *Proc. IEEE Int. Conf. Commun. (ICC)*, Jun. 2014, pp. 4862–4867.
- [58] S. Deng, C. J. Slezak, G. R. MacCartney, Jr., and T. S. Rappaport, "Small wavelengths—Big potential: Millimeter wave propagation measurements for 5G," *Microw. J.*, vol. 57, no. 11, pp. 4–12, 2014.
- [59] G. R. MacCartney, Jr., M. K. Samimi, and T. S. Rappaport, "Omni-directional path loss models in New York City at 28 GHz and 73 GHz," in *Proc. IEEE 25th Int. Symp. Pers. Indoor Mobile Radio Commun. (PIMRC)*, Sep. 2014, pp. 227–231.
- [60] S. Sun, G. R. MacCartney, Jr., M. K. Samimi, and T. S. Rappaport, "Synthesizing omnidirectional antenna patterns, received power and path loss from directional antennas for 5G millimeter-wave communications," in *Proc. IEEE Global Commun. Conf. (GLOBECOM)*, Dec. 2015, pp. 1–7.
- [61] T. S. Rappaport and S. Deng, "73 GHz wideband millimeter-wave foliage and ground reflection measurements and models," in *Proc. IEEE Int. Conf. Commun. Workshop (ICCW)*, Jun. 2015, pp. 1238–1243.
- [62] T. A. Thomas *et al.*, "A prediction study of path loss models from 2–73.5 GHz in an urban-macro environment," in *Proc. IEEE Veh. Technol. Conf. (VTC-Spring)*, May 2016.
- [63] S. Sun *et al.*, "Propagation path loss models for 5G urban micro- and macro-cellular scenarios," in *Proc. IEEE Veh. Technol. Conf. (VTC-Spring)*, May 2016.
- [64] M. Steinbauer, A. F. Molisch, and E. Bonek, "The double-directional radio channel," *IEEE Antennas Propag. Mag.*, vol. 43, no. 4, pp. 51–63, Aug. 2001.
- [65] A. A. M. Saleh and R. A. Valenzuela, "A statistical model for indoor multipath propagation," *IEEE J. Sel. Areas Commun.*, vol. 5, no. 2, pp. 128–137, Feb. 1987.
- [66] Q. Spencer, M. Rice, B. Jeffs, and M. Jensen, "A statistical model for angle of arrival in indoor multipath propagation," in *Proc. IEEE 47th Veh. Technol. Conf. (VTC)*, vol. 3, May 1997, pp. 1415–1419.
- [67] R. B. Ertel, P. Cardieri, K. W. Sowerby, T. S. Rappaport, and J. H. Reed, "Overview of spatial channel models for antenna array communication systems," *IEEE Pers. Commun.*, vol. 5, no. 1, pp. 10–22, Feb. 1998.
- [68] F. Gutierrez, Jr., S. Agarwal, K. Parrish, and T. S. Rappaport, "On-chip integrated antenna structures in CMOS for 60 GHz WPAN systems," *IEEE J. Solid-State Circuits*, vol. 27, no. 8, pp. 1367–1378, Oct. 2009.
- [69] M. K. Samimi, S. Sun, and T. S. Rappaport, "MIMO channel modeling and capacity analysis for 5G millimeter-wave wireless systems," in *Proc. 10th Eur. Conf. Antennas Propag. (EuCAP)*, Apr. 2016, pp. 1–5.
- [70] M. K. Samimi, G. R. MacCartney, Jr., S. Sun, and T. S. Rappaport, "28 GHz millimeter-wave ultrawideband small-scale fading models in wireless channels," in *Proc. IEEE Veh. Technol. Conf. (VTC-Spring)*, May 2016.
- [71] B. Thoma, T. S. Rappaport, and M. D. Kietz, "Simulation of bit error performance and outage probability of  $\Pi/4$  DQPSK in frequency-selective indoor radio channels using a measurement-based channel model," in *Proc. IEEE Global Telecommun. Conf. (GLOBECOM)*, vol. 3, Dec. 1992, pp. 1825–1829.
- [72] C. A. Balanis, *Antenna Theory: Analysis and Design*. Hoboken, NJ, USA: Wiley, 2005.
- [73] T. S. Rappaport, Y. Qiao, J. I. Tamir, J. N. Murdock, and E. Ben-Dor, "Cellular broadband millimeter wave propagation and angle of arrival for adaptive beam steering systems," in *Proc. IEEE Radio Wireless Symp. (RWS)*, Jan. 2012, pp. 151–154.
- [74] T. S. Rappaport, E. Ben-Dor, J. N. Murdock, and Y. Qiao, "38 GHz and 60 GHz angle-dependent propagation for cellular & peer-to-peer wireless communications," in *Proc. IEEE Int. Conf. Commun. (ICC)*, Jun. 2012, pp. 4568–4573.



**Mathew K. Samimi** (S'13) received the B.S. degree in applied physics from the Fu Foundation School of Engineering and Applied Science, Columbia University, New York, NY, USA, in 2012, and the M.S. and Ph.D. degrees in electrical engineering from the Department of Electrical and Computer Engineering, NYU WIRELESS Research Center, New York University Tandon School of Engineering, Brooklyn, NY, USA, in 2014 and 2016, respectively.

His research focuses on developing millimeter-wave statistical spatial channel models for next generation ultrawideband mobile cellular systems for dense urban environments.



**Theodore S. Rappaport** (S'83–M'84–SM'91–F'98) is the David Lee/Ernst Weber Professor of Electrical and Computer Engineering with the New York University (NYU) Tandon School of Engineering, Brooklyn, NY, USA, and the Founding Director of the NYU WIRELESS Research Center. He also holds professorship positions with the Courant Institute of Mathematical Sciences and the NYU Langone School of Medicine. He founded major wireless research centers at the Virginia Polytechnic Institute and State University (MPRG), Blacksburg, VA, USA, The University of Texas at Austin (WNCG), Austin, TX, USA, and at NYU (NYU WIRELESS), and founded two wireless technology companies that were sold to publicly traded firms. He is a highly sought-after technical consultant, having testified before the U.S. Congress and having served the ITU. He has advised more than 100 students, has more than 100 patents issued and pending, and has authored or coauthored several books, including *Wireless Communications: Principles and Practice—Second Edition* (Prentice-Hall, 2002). His latest book, *Millimeter Wave Wireless Communications* (Pearson/Prentice-Hall, 2015), is the first comprehensive text on the subject.